Langtaosha (LTS) Preprint doi: https://doi.org/10.65215/LTSpreprints.2026.02.09.000127. This version posted February 9, 2026. The copyright holder for this preprint (which was not certified by peer review) is the author/funder. Creative Commons license: CC Attribution-NonCommercial-NoDerivatives 4.0 https://creativecommons.org/licenses/by-nc-nd/4.0

ATL2 recruits TRAK1 to promote mitochondrial transport at ER–mitochondria contact sites

Yiru Cheng[1], Peiyuan Chai[1], Xiayuhe Pei[1], Yiwen Chen[2], Xiaoshuai Huang[3], Bei Liu[4], Yiqian Wu[4], Junlin Teng[1]*, Pengli Zheng[1,2,6]*, Jianguo Chen[1,5]*

[1]Key Laboratory of Cell Proliferation and Differentiation of the Ministry of Education, College of Life Sciences, Peking University, Beijing 100871, China.
[2]Center for Life Sciences, Academy for Advanced Interdisciplinary Studies, Peking University, Beijing 100871, China.
[3]Beijing Advanced Center of Cellular Homeostasis and Aging-Related Diseases, Institute of Advanced Clinical Medicine, Peking University, Beijing,100191, China.
[4]National Biomedical Imaging Center, College of Future Technology, Peking University, Beijing 100871, China.
[5]Center for Quantitative Biology, Academy for Advanced Interdisciplinary Studies, Peking University, Beijing 100871, China.
[6]Lead contact.
*Corresponding author. Email: chenjg@pku.edu.cn (J.C.); zhengpl@pku.edu.cn (P.Z.); junlinteng@pku.edu.cn (J.T.)

Abstract

Mitochondrial transport and distribution are crucial for cellular homeostasis, yet whether and how they are regulated by endoplasmic reticulum (ER)–mitochondria contact sites remains unclear. Here, we demonstrate that the ER protein atlastin-2 (ATL2) orchestrates mitochondrial transport and distribution by promoting assembly of the transport machinery at ER–mitochondria contact sites. Mechanistically, ATL2 recruits the adaptor trafficking kinesin-binding protein 1 (TRAK1) to the ER membrane, strengthening the interaction of TRAK1 with the mitochondrial transport adaptor MIRO1 to promote anterograde mitochondrial transport. Loss of ATL2 disrupts this process, leading to perinuclear mitochondrial clustering. We further find that ATL2 stabilizes ER–mitochondria contact sites by interacting with MFN2, providing a platform for mitochondrial transport complex assembly. Moreover, under hypoxia, ATL2 is ubiquitinated at lysine 567 by the E3 ligase SYVN1, leading to its degradation and a resulting defect in mitochondrial distribution. Our findings elucidate a novel ER-mediated mechanism for mitochondrial transport.

Teaser

ATL2, a key regulator at ER–mitochondria contacts, licenses assembly of the anterograde mitochondrial transport machinery.

Langtaosha (LTS) Preprint doi: https://doi.org/10.65215/LTSpreprints.2026.02.09.000127. This version posted February 9, 2026. The copyright holder for this preprint (which was not certified by peer review) is the author/funder. Creative Commons license: CC Attribution-NonCommercial-NoDerivatives 4.0 https://creativecommons.org/licenses/by-nc-nd/4.0

Introduction

Mitochondria are highly dynamic organelles that not only produce cellular energy but also require precise intracellular transport and distribution to support local metabolic demands and maintain overall cellular fitness. Defects in these processes are now widely implicated in the pathogenesis of major human diseases (*1–3*). Mitochondria undergo bidirectional transport along microtubules. The kinesin-1 motor primarily mediates their anterograde transport toward the microtubule plus-end, whereas retrograde movement toward the minus-end is driven by the cytoplasmic dynein–dynactin motor complex (*4, 5*). Kinesin-1 is a heterotetramer composed of two heavy and two light chains, in which the heavy chain N-terminus binds microtubules, and its C-terminus interacts with cargo or light chains (*6, 7*). Mammals express three heavy chain isoforms that exhibit distinct expression patterns: KIF5B is widespread, whereas KIF5A and KIF5C are largely neuron-specific (*8*). A functionally conserved adaptor complex forms the critical link between these motors and mitochondria. The central components are the trafficking kinesin-binding proteins (TRAKs), which recruit these motors to mitochondria via the membrane-anchored GTPase MIRO (*5, 9–11*). The TRAK–MIRO adaptor complex in mammals comprises paralogous pairs, TRAK1/2 and MIRO1/2 (*12–14*). Beyond this core complex, other adaptor proteins, including FEZ1, syntabulin, RanBP2, ARMCX1, ARMCX3, and metaxin, also contribute to mitochondrial motility (*15–17*). A central remaining question is which adaptor combinations are recruited for mitochondrial transport under specific conditions, and how upstream signals regulate this recruitment.

The ER and mitochondria form specialized membrane contact sites, also known as mitochondria-associated ER membranes (MAMs), which are platforms for lipid exchange, calcium signaling, and regulation of mitochondrial dynamics (*18, 19*). Many proteins have been identified as membrane tethers at ER–mitochondria contact sites (*20*). Among these, the mitochondrial fusion protein mitofusin 2 (MFN2) forms interorganellar tethers through homotypic or heterotypic interactions with MFN1or MFN2 (*21, 22*). Given the persisting uncertainty regarding the ER localization of MFN2, it is plausible that additional, yet unidentified, ER-resident proteins cooperate with MFN2 to facilitate this interorganellar tethering. Beyond these established roles, ER–mitochondria contact sites also regulate mitochondrial transport (*23*), yet the precise mechanisms underlying this coordination remain unclear.

The dynamin-like GTPase atlastin (ATL) is the master regulator of ER membrane fusion (*24, 25*). Mammals express three paralogs with distinct expression patterns: brain-enriched ATL1 and the ubiquitously expressed ATL2 and ATL3 (*26*). Beyond their canonical ER fusion activity, ATL proteins also exhibit membrane-tethering capabilities (*27, 28*). The physiological significance of the ATL family is demonstrated by its disease associations, ranging from genetic mutations of ATL1 and ATL3 in hereditary neurodegenerative diseases to elevated ATL2 expression in models of Alzheimer's disease (*29–31*). Furthermore, embryonic lethality and cerebellar defects in *ATL2*-knockout mice demonstrate its critical role in development (*32*). Although mitochondrial transport deficits in ATL1-mutant patient-derived cells indicate a role for ATLs in regulating mitochondrial motility (*33*), the mechanistic basis of this involvement remains elusive.

In this study, we demonstrate that ATL2 regulates mitochondrial transport by recruiting TRAK1 to promote assembly of the TRAK1–MIRO1 complex. Furthermore, we show that ATL2–MFN2 interactions reinforce organelle tethering, creating a structural platform for mitochondrial transport. Finally, we reveal that hypoxia disrupts this process by promoting ubiquitin-dependent degradation of ATL2. Our work thus provides a mechanistic framework for understanding how ER–mitochondria contact sites govern mitochondrial transport.

Langtaosha (LTS) Preprint doi: https://doi.org/10.65215/LTSpreprints.2026.02.09.000127. This version posted February 9, 2026. The copyright holder for this preprint (which was not certified by peer review) is the author/funder. Creative Commons license: CC Attribution-NonCommercial-NoDerivatives 4.0 https://creativecommons.org/licenses/by-nc-nd/4.0

Results

ATL2 promotes mitochondrial anterograde transport and proper distribution

To investigate whether ATL2 regulates mitochondrial transport, we first generated *ATL2* knockout (KO) in COS-7 cells, which do not endogenously express ATL1 (*34*). In *ATL2* KO cells, mitochondria were prominently clustered around the nucleus, whereas in *ATL3* KO cells, mitochondrial distribution was dispersed and similar to that in wild-type (WT) cells (Fig. 1, A and B). To quantitatively assess this phenotype, we used the mitochondrial mean distribution radius (MDR) assay as previously described (*35*), which reflects the average distance of mitochondria from the nuclear envelope to the plasma membrane (higher MDR values indicate more peripheral localization). Consistent with the morphological observations, *ATL2* KO cells, but not *ATL3* KO cells, showed a significantly smaller MDR than WT cells (Fig. 1C).

ATL2 deletion leads to aberrant ER morphology, characterized by reduced tubule branching. Re-expression of ATL3 rescues this ER structural defect because of functional redundancy among ATL family members in ER shaping (*36*). Consistent with those findings, re-expression of either ATL2 or ATL3 in *ATL2* KO cells restored normal ER morphology. However, only re-expression of ATL2 reversed the perinuclear mitochondrial clustering phenotype, whereas ATL3 re-expression failed to rescue mitochondrial distribution despite correcting ER structure (Fig. 1, B and C). To extend these findings to another cell line, we analyzed mitochondrial distribution in HeLa cells and confirmed the perinuclear clustering of mitochondria in *ATL2* KO HeLa cells (fig. S1, A to C).

To further exclude the possibility that the mitochondrial distribution defect in *ATL2* KO cells is an indirect consequence of altered ER morphology, we generated KO cell lines targeting additional ER-shaping proteins (RTN4, lunapark, and CLIMP63) in COS-7 cells (fig. S1D). As previously reported (*37–39*), deletion of these proteins caused distinct ER morphological abnormalities compared to WT cells; however, none affected mitochondrial distribution (Fig. 1, D and E). These results indicate that, among proteins involved in ER morphology, ATL2 specifically regulates mitochondrial distribution, independent of its established role in ER shaping.

Immunoblotting for the mitochondrial matrix protein HSP60 and the outer membrane protein TOM20 showed comparable expression levels in WT and *ATL2* KO COS-7 cells (fig. S1, E and F). Similarly, immunoblotting analysis in HeLa cells showed that the levels of HSP60, TOM20, and the inner membrane protein TIM50 were unaffected by ATL2 deletion (fig. S1, G and H). These data demonstrate that the perinuclear clustering of mitochondria resulting from ATL2 deletion is not because of a reduction in mitochondrial mass.

To test whether ATL2 deletion alters mitochondrial transport, we labeled mitochondria to visualize and track their dynamics in WT and *ATL2* KO COS-7 cells. We observed significantly fewer mitochondrial anterograde transport events upon ATL2 deletion, with no significant effect on retrograde mitochondrial transport, resulting in perinuclear mitochondrial clustering (Fig. 1F and fig. S1, I and J). Therefore, the ER-resident protein ATL2 emerges as a regulator of mitochondrial distribution, likely by modulating anterograde mitochondrial transport.

ATL2 promotes mitochondrial transport and distribution in a KIF5B-dependent manner

KIF5B is a ubiquitously expressed kinesin-1 motor essential for anterograde mitochondrial transport and is required for peripheral mitochondrial distribution. Loss of KIF5B function causes perinuclear clustering of mitochondria (*40*). We identified an interaction between ATL2 and KIF5B using co-immunoprecipitation and glutathione S-transferase (GST) pull-down assays (Fig. 2, A to C, and fig. S2A). Domain mapping revealed that ATL2 binds the KIF5B tail domain (residues 745–963) (fig. S2, B and C), which coincides with the known binding site for TRAK adaptor proteins (*41*).

Langtaosha (LTS) Preprint doi: https://doi.org/10.65215/LTSpreprints.2026.02.09.000127. This version posted February 9, 2026. The copyright holder for this preprint (which was not certified by peer review) is the author/funder. Creative Commons license: CC Attribution-NonCommercial-NoDerivatives 4.0 https://creativecommons.org/licenses/by-nc-nd/4.0

To test whether ATL2 depends on KIF5B to regulate mitochondrial transport, we generated *KIF5B* KO and *ATL2/KIF5B* double-knockout (DKO) COS-7 and HeLa cell lines using CRISPR/Cas9 approach (fig. S2D). In both cell lines, loss of either ATL2 or KIF5B caused comparable perinuclear mitochondrial clustering. The DKO cells showed no further enhancement of this phenotype (Fig. 2, D and E, and fig. S2, E and F). While ATL2 re-expression rescued mitochondrial distribution in *ATL2* KO cells, it did not in the *ATL2/KIF5B* DKO background (Fig. 2, D and E, and fig. S2, E and F). This observation suggests that ATL2 operates through a KIF5B-dependent pathway to control mitochondrial positioning.

ATL2 cooperates with the TRAK1 adaptor to orchestrate mitochondrial distribution

TRAK1 and TRAK2 are key adaptors for mitochondrial transport, with TRAK1 preferentially binding KIF5B, which is critical for anterograde mitochondrial trafficking (*5, 7*). TRAK1 loss or dominant-negative mutant expression disrupts mitochondrial transport (*9*). To explore the functional link between ATL2 and TRAK1, we examined their interaction. Co-immunoprecipitation assays confirmed that endogenous and overexpressed ATL2 associate with TRAK1 (Fig. 3, A and B, and fig. S3A). Further, *in vitro* pull-down assays using purified GST-TRAK1 and the His-tagged cytosolic domain of ATL2 (6×His-cytoATL2, residues 1–476) suggested a direct physical interaction between the two proteins (Fig. 3C). Domain mapping analyses (fig. S3, B to E) revealed that ATL2 interacts with TRAK1 via its GTPase domain (residues 57–373), whereas TRAK1 binds ATL2 through a C-terminal region (residues 658–953), a site distinct from those mediating TRAK1 interactions with KIF5B or the mitochondrial receptor MIRO1 (*5, 42*). Among ATL family homologs, ATL2 and ATL1 interacted with TRAK1, whereas ATL3 did not (Fig. 3D and fig. S3F). This binding specificity is consistent with our observations that *ATL2* KO caused perinuclear mitochondrial clustering, whereas *ATL3* KO did not (Fig. 1B and fig. S1B), indicating that TRAK1 binding correlates with ATL protein function in mitochondrial distribution. In addition, overexpressed TRAK1 colocalized with ATL2 in cells (fig. S3G), supporting their physiological association. Moreover, we used a proximity ligation assay (PLA) to visualize the association between TRAK1 and the ER. ER association of TRAK1 decreased substantially upon ATL2 deletion (Fig. 3, E and F), indicating that ATL2 is essential for TRAK1 association with the ER.

To determine the functional relationship between ATL2 and TRAK1 in mitochondrial transport, we overexpressed TRAK1 in WT and *ATL2* KO HeLa cells and assessed mitochondrial distribution. In WT cells, TRAK1 overexpression significantly increased mitochondrial distribution at the cell periphery (Fig. 3, G and H). This effect was abolished in ATL2-deficient cells (Fig. 3, G and H). These results indicate that ATL2 is required for TRAK1 to promote mitochondrial transport to the plasma membrane.

To determine whether ATL2 regulates the TRAK1–KIF5B interaction, co-immunoprecipitation assays were performed in TRAK1-expressing WT and *ATL2* KO HeLa cells. The association between TRAK1 and KIF5B remained unchanged upon ATL2 depletion (fig. S3H). Conversely, the interaction between ATL2 and KIF5B depended on TRAK1, as TRAK1 depletion abolished ATL2–KIF5B binding (fig. S3I), indicating that ATL2 associates with KIF5B indirectly via TRAK1.

ATL2 promotes the interaction between TRAK1 and MIRO1

MIRO proteins, which anchor to the outer mitochondrial membrane and recruit TRAK adaptors (*10, 14*), co-immunoprecipitated with overexpressed ATL2 (Fig. 3I). To determine whether ATL2 and MIROs operate in a common pathway, MIRO1 and MIRO2 were depleted in *ATL2* KO cells (fig. S3J). This double deficiency did not exacerbate the mitochondrial distribution defects in *ATL2* KO cells (Fig. 3, J and K, and fig. S3, K and L), placing ATL2 and MIROs within the same functional pathway.

Langtaosha (LTS) Preprint doi: https://doi.org/10.65215/LTSpreprints.2026.02.09.000127. This version posted February 9, 2026. The copyright holder for this preprint (which was not certified by peer review) is the author/funder. Creative Commons license: CC Attribution-NonCommercial-NoDerivatives 4.0 https://creativecommons.org/licenses/by-nc-nd/4.0

We next asked whether ATL2 regulates the interactions between TRAK1 and MIROs. Co-immunoprecipitation assays in TRAK1-expressing WT and *ATL2* KO HeLa cells showed a marked decrease in the TRAK1–MIRO1 interaction upon ATL2 loss, despite unchanged TRAK1–MIRO2 association (Fig. 3, L and M, and fig. S3H). This specificity was confirmed *in vitro*, where ATL2 directly increased the binding between recombinant TRAK1 and MIRO1 (Fig. 3, N and O). Thus, ATL2 is specifically required to stabilize the TRAK1–MIRO1 interaction.

ATL2 is required for maintaining ER–mitochondria contact sites

Since ATL2 is an ER membrane protein, we reasoned that it might regulate mitochondrial transport via ER–mitochondria contact sites. To test this, we performed density gradient centrifugation (*43*), and confirmed an accumulation of ATL2 in MAM fractions from mouse liver (Fig. 4A). To provide ultrastructural confirmation, we used immunoelectron microscopy, which verified that ATL2 localizes to ER–mitochondria contact sites (Fig. 4B).

We next performed PLA using antibodies against the ER protein calnexin and the mitochondrial outer membrane protein TOM20 to examine the effects of ATL2 on ER–mitochondria contact sites. Deletion of ATL2, but not ATL3, significantly reduced the number of PLA-positive puncta, an effect that was rescued by ATL2 re-expression (Fig. 4, C and D, and fig. S4, A and B). In addition, we validated the role of ATL2 in regulating ER–mitochondria contact sites using a split-GFP-based contact site sensors (SPLICS) system (*44*). ATL2 loss, in contrast to ATL3, markedly decreased the SPLICS signal, a reduction that was reversed upon ATL2 reintroduction (Fig. 4, E and F, and fig. S4, C and D). Together, these results establish a specific requirement for ATL2 in maintaining ER–mitochondria contact sites.

The ATL2–MFN2 interaction is required for mitochondrial transport

Beyond its established role in mediating ER–mitochondria tethering (*21*), MFN2 is also linked to the regulation of mitochondrial transport (*45*). We generated *MFN1* or *MFN2* KO lines in COS-7 and HeLa cells (fig. S5A) and validated that loss of MFN2, but not MFN1, caused perinuclear clustering of mitochondria (fig. S5, B and C). We therefore investigated whether MFN2 collaborates with ATL2 to regulate mitochondrial transport. Co-immunoprecipitation experiments in HEK293T cells confirmed the interaction between ATL2 and MFN2 (Fig. 5A). This binding was specific to ATL2 and ATL1, as MFN2 did not bind ATL3 (Fig. 5B and fig. S5D). The interaction was further validated under endogenous conditions and shown to be direct by *in vitro* pull-down assays (Fig. 5, C and D, and fig. S5, E and F). Next, immunoprecipitation analyses revealed that ATL2 interacted with MFN2 through its GTPase domain (residues 57–373) (fig. S5G).

As the Charcot–Marie–Tooth type 2A-associated MFN2 R94Q mutation disrupts ER–mitochondria contact sites and impairs mitochondrial transport (*46*), we investigated whether this pathogenic variant alters its interaction with ATL2. The MFN2 R94Q mutant displayed substantially reduced binding to mEmerald-ATL2 than WT MFN2 in co-immunoprecipitation assays (Fig. 5, E and F). The MFN2 R94Q mutant consistently failed to restore normal mitochondrial distribution in *MFN2* KO and *MFN2/ATL2* DKO cells, unlike WT MFN2 (Fig. 5, G and H, and fig. S5, H to K). These results indicate that the ATL2–MFN2 interaction is essential for proper mitochondrial distribution.

We hypothesized that the ATL2–MFN2 complex acts as a tether between the ER and mitochondria. To test this, we used a PLA to quantify ER–mitochondria contact sites. Deletion of both proteins in HeLa cells significantly reduced PLA signals, a phenotype rescued by WT ATL2 and WT MFN2, but not by the interaction-deficient MFN2 R94Q mutant (Fig. 5, I and J). Thus, a functional ATL2–MFN2 complex is required to maintain ER–mitochondria contact sites. We next investigated whether MFN2, through its role in ER–mitochondria tethering, influences the TRAK1–MIRO1 interaction. MFN2 deletion weakened the TRAK1–MIRO1 interaction (Fig. 5,

Langtaosha (LTS) Preprint doi: https://doi.org/10.65215/LTSpreprints.2026.02.09.000127. This version posted February 9, 2026. The copyright holder for this preprint (which was not certified by peer review) is the author/funder. Creative Commons license: CC Attribution-NonCommercial-NoDerivatives 4.0 https://creativecommons.org/licenses/by-nc-nd/4.0

K and L). Furthermore, the interaction between ATL2 and MIRO1 was inhibited upon MFN2 loss (Fig. 5M). Together, these results reveal that the ATL2–MFN2 tether couples ER–mitochondria contact sites to the mitochondrial transport machinery by stabilizing the TRAK1–MIRO1 interaction, thereby being essential for proper mitochondrial distribution.

Hypoxia induces ATL2 degradation and leads to clustered mitochondria

Perinuclear clustering of mitochondria has been observed in capillary endothelial cells of rat under hypoxia (*47*), yet the underlying molecular mechanism remains unclear. In COS-7 and HeLa cells, hypoxia-induced perinuclear clustering of mitochondria coincided with a specific decrease in ATL2 protein levels (Fig. 6, A to D, and fig. S6, A to D); whereas the expression of ATL3, CNX, and TOM20 remained stable (Fig. 6, C and D, and fig. S6, C and D), suggesting that ATL2 degradation is a potential mechanism. Hypoxia-induced ATL2 degradation was prevented by the proteasome inhibitor MG132 but not by the autophagy inhibitor chloroquine (Fig. 6E and fig. S6E), indicating that it is ubiquitin-proteasome-mediated. This was further supported by increased ATL2 ubiquitination under hypoxia, which was increased by MG132 (Fig. 6F), demonstrating that hypoxia triggers proteasome-dependent degradation of ATL2.

To identify the residue responsible for hypoxia-induced degradation, we performed mass spectrometry-based ubiquitination profiling and identified lysine 567 (K567) as a potential hypoxia-induced ubiquitination site in ATL2 (fig. S6F). Mutation of K567 to arginine (K567R) inhibited ATL2 degradation in response to hypoxic treatment (Fig. 6, G and H, and fig. S7, A and B). Consistent with this, ubiquitination of the K567R mutant was decreased under hypoxia compared with WT ATL2 (Fig. 6I). The K567R mutation also prevented the hypoxia-induced perinuclear clustering of mitochondria (Fig. 6, J and K, and fig. S7, C and D). These data demonstrate that ubiquitination of K567 is the key signal triggering ATL2 degradation and subsequent mitochondrial perinuclear clustering under hypoxia.

We next evaluated mitochondrial function under hypoxia. Hypoxia induced a marked increase in mitochondrial reactive oxygen species (ROS) in cells expressing WT ATL2, whereas the K567R mutant effectively suppressed this ROS elevation (Fig. 6, L and M). Concomitantly, the hypoxia-induced reduction in mitochondrial membrane potential was rescued by the K567R mutant (Fig. 6N and fig. S7E).

SYVN1 is responsible for ATL2 ubiquitination under hypoxia

ER-localized E3 ubiquitin ligase synoviolin 1 (SYVN1) ubiquitinates ATL family proteins (*48*). Co-immunoprecipitation assays confirmed the association between SYVN1 and ATL2 (Fig. 7, A and B). *In vitro* pull-down assays showed that purified GST-SYVN1 directly bound to ATL2, demonstrating a direct interaction between SYVN1 and ATL2 (Fig. 7C). Overexpression of WT SYVN1, but not its catalytically inactive C329S mutant (*48*), markedly increased ATL2 ubiquitination (Fig. 7D). The K567R mutation of ATL2 abolished SYVN1-induced ATL2 ubiquitination (Fig. 7E). Pharmacological inhibition of SYVN1 by LS-102 (*49*) prevented hypoxia-induced ubiquitination and degradation of ATL2 (Fig. 7, F to H). Consequently, SYVN1 inhibition also rescued aberrant perinuclear mitochondrial clustering observed under hypoxia (Fig. 7, I and J), demonstrating that SYVN1 is critically involved in hypoxia-induced ATL2 degradation. Taken together, these data establish that hypoxia promotes SYVN1-mediated ubiquitination of ATL2 at K567, leading to its proteasomal degradation and disruption of mitochondrial distribution.

Discussion

Communication between the ER and mitochondria is crucial for cellular homeostasis, with their contact sites serving as hubs for calcium transfer, lipid exchange, and mitochondrial fission (*18, 19*). Extending beyond these roles, a key unresolved question is whether these contact sites also

Langtaosha (LTS) Preprint doi: https://doi.org/10.65215/LTSpreprints.2026.02.09.000127. This version posted February 9, 2026. The copyright holder for this preprint (which was not certified by peer review) is the author/funder. Creative Commons license: CC Attribution-NonCommercial-NoDerivatives 4.0 https://creativecommons.org/licenses/by-nc-nd/4.0

regulate mitochondrial transport. These two organelles associate during movement and co-localize on acetylated microtubules (*50*). The transport regulator MIRO1 is detected at these contact sites, and its yeast ortholog Gem1 is a component of the ER–mitochondria encounter structure tethering complex (*51*). Furthermore, the ER protein REEP5 interacts with MFN1/2, promoting coupled organellar movement (*52*). Nevertheless, the molecular machinery underlying ER-mediated regulation of mitochondrial transport along microtubules is undefined. Here, we report that ER–mitochondria contact sites are a platform for orchestrating mitochondrial transport. ATL2 recruits the cytosolic adaptor TRAK1 to the ER through its GTPase domain, while its interaction with mitochondrial MFN2 establishes a membrane-tethering platform. This collaborative assembly promotes the formation of the TRAK1–MIRO1 complex to drive anterograde mitochondrial transport (Fig. 8). Furthermore, we link this mechanism to the hypoxic response, in which ubiquitination at K567 dismantles ATL2, impairing mitochondrial transport and causing perinuclear clustering.

The ATL GTPases exhibit distinct tissue distributions. ATL1 is found predominantly in the brain, whereas ATL2 and ATL3 are more enriched in non-neuronal tissues (*26*). ATL2 expression is particularly high in muscle (*32*). This expression pattern aligns with our findings that ATL2 governs mitochondrial transport and distribution, processes essential for the function of this high-energy-demand tissue. Despite high sequence conservation, ATL3 cannot bind TRAK1 or MFN2, whereas ATL2 interacts with both (Fig. 3D and 5B); ATL1, which shares greater sequence homology with ATL2 (*53*), also interacts with TRAK1 and MFN2 (fig. S3F and S5D), indicating functional divergence among homologs. Mutations in the *ATL1* gene are a well-established genetic cause of hereditary spastic paraplegia, a neurodegenerative disease (*29*). In a disease-relevant model, forebrain neurons differentiated from patient-derived pluripotent stem cells carrying the ATL1 P342S mutation exhibit impaired mitochondrial transport (*33*). Whether ATL1 regulates neuronal mitochondrial transport via an ATL2-like mechanism remains an important question, the answer to which would advance understanding the pathology of hereditary spastic paraplegia.

Our findings position ATL2 as a molecular scaffold that coordinates assembly of the mitochondrial transport machinery. We identified a specific C-terminal domain (residues 658–953) in TRAK1 that mediates its recruitment to the ER by ATL2 (fig. S3, D and E), distinct from its MIRO1-binding regions (*42*). This spatially constrained recruitment facilitates efficient transfer of TRAK1 to mitochondrial MIRO1 at ER–mitochondria contact sites, thereby promoting transport complex assembly and driving anterograde mitochondrial transport. The essential role of this ATL2-mediated platform is underscored by the disruption of TRAK1–MIRO1 interaction upon ATL2 depletion and its potent increase upon reconstitution with recombinant ATL2 *in vitro* (Fig. 3, L to O). We propose that the ATL2–MFN2 tether structurally aligns the organelles, enabling this precise molecular handover. It remains to be determined whether TRAK1 and MFN2 compete for an overlapping binding site on the ATL2 GTPase domain or associate with distinct epitopes, and which specific signals define the spatiotemporal context for initiating TRAK1 transfer.

The role of MFN2 as an ER–mitochondria tether, bridging organelles via homotypic or heterotypic interactions (*21, 54*), is conceptually appealing but limited by unresolved questions regarding its ER localization. We identified the ER-resident GTPase ATL2 as an essential partner that functionally and physically couples with mitochondrial MFN2. First, ATL2 is enriched at ER–mitochondria contact sites, and its deletion reduces contact site abundance (Fig. 4 and fig. S4). Furthermore, ATL2 directly interacts with mitochondrial MFN2 (Fig. 5D). Importantly, this the MFN2 R94Q pathogenic variant disrupts this interaction, providing a molecular explanation for the observed contact site deficiency (Fig. 5, E to J, and fig. S5, J and K). Collectively, these data establish the ATL2–MFN2 heterocomplex as a fundamental tether. Future work will

Langtaosha (LTS) Preprint doi: https://doi.org/10.65215/LTSpreprints.2026.02.09.000127. This version posted February 9, 2026. The copyright holder for this preprint (which was not certified by peer review) is the author/funder. Creative Commons license: CC Attribution-NonCommercial-NoDerivatives 4.0 https://creativecommons.org/licenses/by-nc-nd/4.0

elucidate the regulatory mechanisms governing this complex and its potential interactions with other tethering proteins.

Materials and Methods

Plasmids construction and reagents

The plasmids pSIN, psPAX2, and PMD2.G related to lentivirus production were gifts from Dr. Jiang Zhengfan (College of Life Sciences, Peking University, Beijing, China). mEmerald-Sec61β was a gift from Dr. Dong Li (Institute of Biophysics, Chinese Academy of Sciences, Beijing, China). The sequences encoding human ATL2, ATL3, TRAK1, MFN2, MIRO1, KIF5B, and SYVN1 were amplified from a HEK293T cell cDNA library by PCR and cloned into the pSIN, p3×FLAG-CMV-7.1 (Sigma-Aldrich, E7533), p3×FLAG-CMV-14 (Sigma-Aldrich, E7908), pcDNA3.1 (+) (Invitrogen, V79020), mEmerald-C1 (Addgene, 53975), N1-mScarlet (Addgene, 85054), pCold-MBP (NovoPro Bioscience Inc., V012984), pET-28a (+) (Novagen, 69864), or pGEX-6P-1 (GE Healthcare, 28-9546-48) vectors. Mutations in ATL2, MFN2, and SYVN1 were generated using PCR site-directed mutagenesis. SPLICS Mt-ER Long P2A (Addgene, 164107) was purchased from Addgene.

Chloroquine (C6628), MG132 (M8699), puromycin (P8833), and the Duolink In Situ PLA kit (DUO92002, DUO92004, DUO92008, DUO92013) were obtained from Sigma-Aldrich. Blasticidin (S7419) was obtained from Selleckchem. LS-102 (HY-135844) was purchased from MedChemExpress.

Antibodies

Primary antibodies used were rabbit polyclonal anti-ATL2 (Proteintech, 16688-1-AP; immunoblot, 1:1,000), rabbit polyclonal anti-ATL3 (Proteintech, 16921-1-AP; immunoblot, 1:1,000), mouse monoclonal anti-CLIMP63 (Enzo Life Sciences, ENZ-ABS669; immunoblot, 1:1,000), rabbit polyclonal anti-Calnexin (Proteintech, 10427-2-AP; immunoblot, 1:5,000, immunofluorescence, 1:500), mouse monoclonal anti-Calnexin (Proteintech, 66903-1-Ig; immunofluorescence, 1:500), rabbit polyclonal anti-Flag (Proteintech, 20543-1-AP; immunofluorescence, 1:200), mouse monoclonal anti-Flag (Sigma-Aldrich, F1804, clone M2; immunoblot, 1:5,000, immunofluorescence, 1:500), rabbit polyclonal anti-GFP (Proteintech, 50430-2-AP; immunoblot, 1:3,000, immunofluorescence, 1:300), mouse monoclonal anti-GAPDH (Proteintech, 60004-1-AP; immunoblot, 1:20,000), mouse monoclonal anti-HA (Sigma-Aldrich, H9658, clone HA-7; immunoblot, 1:10,000), rabbit polyclonal anti-HIF1α (Proteintech, 20960-1-AP; immunoblot, 1:1,000), mouse monoclonal anti-His (Abmart, M20001; immunoblot, 1:10,000), rabbit polyclonal anti-HSP60 (Proteintech, 15282-1-AP; immunoblot, 1:2,000), rabbit polyclonal anti-KIF5B (Proteintech, 21632-1-AP; immunoblot, 1:2,000), rabbit polyclonal anti-Lunapark (Abcam, Ab121416; immunoblot, 1:500), rabbit polyclonal anti-MFN1 (Proteintech, 13798-1-AP; immunoblot, 1:1,000), rabbit monoclonal anti-MFN2 (Cell Signaling Technology, 9482S; immunoblot, 1:10,000), mouse monoclonal anti-MIRO1 (Sigma-Aldrich, WH0055288M1; immunoblot, 1:1,000), rabbit polyclonal anti-MIRO2 (Proteintech, 11237-1-AP; immunoblot, 1:1,000), rabbit polyclonal anti-RTN4 (Novus Biologicals, NB100-56681; immunoblot, 1:1,000), rabbit polyclonal anti-SYVN1 (Proteintech, 13473-1-AP; immunoblot, 1:1,000), mouse monoclonal anti-TIM50 (Santa Cruz Biotechnology, sc-393678; immunoblot, 1:1,000), mouse monoclonal anti-TOM20 (BD Biosciences, 612278; immunofluorescence, 1:500), rabbit polyclonal anti-TOM20 (Proteintech, 11802-1-AP; immunoblot, 1:5,000, immunofluorescence, 1:500), rabbit polyclonal anti-ubiquitin (Proteintech, 10201-2-AP; immunoblot, 1:1,000), mouse monoclonal anti-V5 (Thermo Fisher Scientific, R960-25; immunoblot, 1:5,000), mouse monoclonal anti-α-tubulin (Sigma-Aldrich, T6199, clone DM1A, immunoblot, 1:10,000, immunofluorescence, 1:1,000), and mouse monoclonal anti-β-actin (Proteintech, 66009-1-Ig, clone 2D4H5, immunoblot, 1:20,000). Horseradish peroxidase-

Langtaosha (LTS) Preprint doi: https://doi.org/10.65215/LTSpreprints.2026.02.09.000127. This version posted February 9, 2026. The copyright holder for this preprint (which was not certified by peer review) is the author/funder. Creative Commons license: CC Attribution-NonCommercial-NoDerivatives 4.0 https://creativecommons.org/licenses/by-nc-nd/4.0

conjugated goat anti-rabbit or anti-mouse secondary antibodies were purchased from Jackson ImmunoResearch. Alexa Fluor 488/568/647-conjugated goat anti-mouse IgG (H+L) or 568-conjugated goat anti-rabbit IgG (H+L) highly cross-adsorbed secondary antibodies were obtained from Invitrogen.

Cell culture and transfections

COS-7, HeLa, and HEK293T cells were grown in high-glucose Dulbecco's modified Eagle medium (DMEM, Cellmax, CGM101.06) supplemented with 10% fetal bovine serum (FBS, Cellmax, SA201.02) under 5% CO_2 at 37 ℃. For hypoxia treatment, cells were cultured in a hypoxic chamber (Billups-Rothenberg) with 1% O_2, 5% CO_2, and 94% N_2 at 37 ℃. Polyethylenimine (Polysciences, 23966) was used to transfect HEK293T cells. COS-7 and HeLa cells were transfected with Lipofectamine 3000 (Thermo Fisher Scientific, L3000015) according to the manufacturer's instructions.

Immunoblotting

Samples were boiled at 100 ℃ for 8 min, separated on 4%–12% Bis-Tris gels (GenScript), and transferred to polyvinylidene difluoride membranes (Millipore, IPVH00010). Membranes were blocked with 4% (w/v) skim milk powder in Tris-buffered saline containing 0.1% Tween-20 (TBST) for 20 min at room temperature. After blocking, the membranes were incubated with primary antibodies diluted in blocking buffer for 1.5 h at room temperature, followed by TBST washes. Membranes were then probed with horseradish peroxidase-conjugated secondary antibodies for 1.5 h at room temperature. Following washing with TBST, immunoreactive bands were detected by enhanced chemiluminescence and captured on X-ray film in a darkroom. Immunoblot band intensities were quantified using ImageJ software (National Institutes of Health).

Immunofluorescence and live-cell imaging

For immunofluorescence, cells cultured on glass coverslips were washed twice with PBS and fixed with 4% (w/v) paraformaldehyde at 37 °C for 15 min. After three washes with PBS, cells were permeabilized with 0.15% Triton X-100 in PBS for 9 min at room temperature and then washed three times with PBS. Blocking was performed using 4% BSA in PBS for 30 min at room temperature. Cells were then incubated with primary antibodies diluted in blocking buffer for 1.5 h at room temperature. Following three PBS washes, cells were incubated with secondary antibodies for 1.5 h at room temperature, with or without DAPI (Invitrogen, D1306). After three final PBS washes, coverslips were mounted using Fluoromount-G (SouthernBiotech, 0100-01) and stored overnight at 4 °C. Images were acquired using a Leica TCS SP8 confocal system with a 63×/1.4 NA or 100×/1.4 NA oil-immersion objective, a ZEISS LSM 980 confocal microscope with Airyscan and a 63×/1.4 NA oil-immersion objective, or a Live SR CSU W1 spinning disk confocal system equipped with a 100×/1.4 NA oil-immersion objective. Image analysis was performed using ZEN (Zeiss) or ImageJ.

For live-cell imaging, COS-7 cells in glass-bottom dishes (Cellvis, D35-20-1.5-N) were incubated with 125 nM PK Mito Deep Red (Genvivo, PKMDR-2) at 37 °C for 45 min for mitochondrial labeling. Live-cell imaging was performed on a High Sensitivity Structured Illumination Microscope (HIS-SIM; Guangzhou Computational Super-resolution Biotech) equipped with a 100×/1.5 NA oil-immersion objective, using IMAGER software in 2D-SIM-2 mode. Time-lapse acquisition was performed for 10 min with 2-s intervals. Acquired images were first reconstructed using Wiener Deconvolution to generate super-resolution images, followed by Sparse Deconvolution with MicroscopeX FINER software.

Langtaosha (LTS) Preprint doi: https://doi.org/10.65215/LTSpreprints.2026.02.09.000127. This version posted February 9, 2026. The copyright holder for this preprint (which was not certified by peer review) is the author/funder. Creative Commons license: CC Attribution-NonCommercial-NoDerivatives 4.0 https://creativecommons.org/licenses/by-nc-nd/4.0

Quantification of mitochondrial distribution

Mitochondrial distribution was quantified following an established method for ER distribution (*35*). Confocal images were processed in ImageJ, in which the cell center was identified from the DAPI signal (channel 1), and the cell boundary was defined using microtubule or ER markers (channel 3). Mitochondrial signals (channel 2) and reference signals were extracted and exported to MATLAB for computational analysis. The analysis generated 3,600 radial segments at 0.1° intervals from the cell center to the farthest peripheral point. Fluorescence intensities of both nuclear and mitochondrial signals along each radius were normalized. The mean distribution radius (MDR) was calculated as the average distance of mitochondria between the nuclear envelope and the plasma membrane, with higher MDR values indicating increased peripheral mitochondrial localization.

Reactive oxygen species (ROS)

HeLa cells grown on coverslips were washed with PBS and stained with 100 μM MitoTracker Red CMXRos (Invitrogen, M7512) at 37 °C for 30 min. After three PBS washes, cells were fixed and mounted for microscopic imaging. Representative images were acquired using a Leica TCS SP8 confocal microscope with a 100×/1.4 NA oil-immersion objective. For quantitative analysis, images were acquired using a Live SR CSU-W1 spinning disk confocal system equipped with a 100×/1.4 NA oil-immersion objective. Mean fluorescence intensity of MitoTracker Red signals was quantified using ImageJ.

Mitochondrial membrane potential assay

Cells were seeded in CellCarrier-96 Ultra microplates (PerkinElmer, 6055302) and cultured under normoxic or hypoxic conditions. After washing with PBS, cells were incubated with 2.5 μg/mL JC-1 (Yeasen, 40705ES03) for 20 min at 37 °C. Following two PBS washes, the probe solution was replaced with fresh culture medium. Representative images were acquired using a Leica TCS SP8 confocal microscope with a 100×/1.4 NA oil-immersion objective. For quantification, images were obtained using an Operetta CLS high-content analysis system (PerkinElmer) equipped with a 20×/1.0 NA automated water-immersion objective. Mean fluorescence intensity of JC-1 aggregates (red) and monomers (green) was quantified using ImageJ.

Lentivirus production and stable cell lines

For lentivirus production, HEK293T cells were transfected via polyethylenimine with the packaging plasmid psPAX2, the envelope plasmid pMD2.G, and the indicated transfer plasmids. After 6 h, the medium was replaced with DMEM supplemented with 20% fetal bovine serum. Viral supernatant was harvested 48 h later, filtered through a 0.22 μm membrane (Millipore), and concentrated by adding one-third volume of 40% (w/v) PEG8000, followed by gentle mixing overnight at 4 °C. Viral particles were pelleted by centrifugation and then resuspended in a small volume of DMEM for storage at −80 °C. For infection, target cells were incubated with concentrated virus and 8 μg/mL polybrene (Sigma-Aldrich, 107689). The medium was refreshed 24 h post-infection. To generate stable cell lines, cells were selected with appropriate antibiotics starting 48 h after infection. For fluorescence-based sorting, cells were prepared and sorted by flow cytometry (MoFlo Astrios EQ, Beckman Coulter).

CRISPR/Cas9 gene editing

Knockout cell lines in COS-7 and HeLa cells were generated using the CRISPR/Cas9 system. The targets sequences used were: 5′-GCTTAGATACATGTATAACA-3′ and 5′-AGAGTATGGAAGACTTGCGA-3′ for ATL2; 5′-GTGGCAGCAGCTGCCTCAAG-3′ and 5′-AGATCTTGATGTGGTGGTGG-3′ for ATL3; 5′-GCATATGGACAAACATCCTC-3′ and 5′-GTTATGGATACCATAGATGA-3′ for KIF5B; 5′-AGTGACAAAGTGCTTAAGTG-3′ and 5′-

Langtaosha (LTS) Preprint doi: https://doi.org/10.65215/LTSpreprints.2026.02.09.000127. This version posted February 9, 2026. The copyright holder for this preprint (which was not certified by peer review) is the author/funder. Creative Commons license: CC Attribution-NonCommercial-NoDerivatives 4.0 https://creativecommons.org/licenses/by-nc-nd/4.0

GGTTACCTATCCAAAGTGAG-3′ for MFN2; 5′-CCTAGTGGGATTGGCCATATAA-3′ and 5′-GCTACTGTGAAAAACATAATGG-3′ for MFN1; 5′-CTAAGTTATTTACCTTGTCC-3′ for Lunapark; 5′-GCCGCGCCCGCCATGCCCTCGG-3′ for CLIMP63; 5′-CATCAGCTTTAGGATATAC-3′ for RTN4; 5′-GTGTGATCTCCTCTTGCTGG-3′ for TRAK1. The oligonucleotides were synthesized, cloned into the lentiCRISPRv2 vector (Addgene, 52961), and delivered via lentiviral transduction. At 48 h post-infection, cells were selected with the appropriate antibiotic. Single-cell clones were isolated by flow cytometry (MoFlo XDP, Beckman Coulter), expanded for approximately two weeks, and then transferred to 24-well plates. A portion of each clone was used for immunoblotting analysis, while the remainder was maintained in culture. Clones exhibiting loss of the target protein, as determined by immunoblotting, were further expanded in 12-well plates and verified by genomic sequencing.

Generation of knockdown cell lines

Gene knockdown was achieved by lentiviral transduction of shRNA constructs cloned into the pLKO.1-puro vector (Addgene, 8453). The targeting sequences used to knockdown the genes were 5′-GCAATCCCAAATCCTTTGAAT-3′ for MIRO1 and 5′-CCCAGAATTCTCAGGGCTCTA-3′ for MIRO2. Following infection, cells were selected with 2 μg/mL puromycin, and knockdown efficiency was validated by immunoblotting.

Co-immunoprecipitation

HeLa or HEK293T cells were lysed in ice-cold buffer (25 mM HEPES, pH 7.4, 0.5% Triton X-100, 150 mM KOAc, and 2 mM MgOAc) supplemented with a protease inhibitor cocktail (Sigma-Aldrich, P8340) for 25 min. Following centrifugation at 12,500*g* for 15 min at 4 °C, the supernatants were incubated with the indicated antibody-conjugated beads for 1.5 h at 4 °C. The beads were then washed four times with lysis buffer, and immunoprecipitated proteins were eluted by boiling and analyzed by immunoblotting.

Subcellular fractionation

Mitochondrial and mitochondria-associated ER membrane (MAM) fractions were isolated from mouse liver using an established differential centrifugation protocol (*43*). Fresh liver tissue was dissected in ice-cold Buffer A (30 mM Tris-HCl, pH 7.4, 0.5% BSA, 0.5 mM EGTA, 75 mM sucrose, and 225 mM mannitol), minced, and homogenized. Nuclei and unbroken cells were removed by repeated centrifugation at 740*g* for 5 min at 4 °C. The supernatant was then centrifuged at 9,000*g* for 10 min to obtain crude mitochondria. The resulting supernatant was centrifuged at 20,000*g* for 30 min, and the subsequent supernatant at 100,000*g* for 1 h (Beckman, 70-Ti rotor). The final pellet contained the ER-enriched fraction, whereas the supernatant constituted the cytosolic fraction. The crude mitochondrial pellet was resuspended in Buffer B (as Buffer A without EGTA) and centrifuged at 10,000*g* for 10 min. The pellet was then resuspended in Buffer C (5 mM HEPES, pH 7.4, 0.5 mM EGTA, and 250 mM mannitol) and layered onto a Percoll solution (25 mM HEPES, pH 7.4, 1 mM EGTA, 30% Percoll, and 225 mM mannitol). After centrifugation at 95,000*g* for 30 min (Beckman, SW40 rotor), the lower (mitochondria) and middle (MAM) bands were collected. Mitochondria were washed by centrifugation at 6,300*g*, and the MAM fraction was pelleted at 100,000*g* for 1 h (70-Ti rotor, Beckman).

Immunoelectron microscopy

Samples for immunoelectron microscopy were prepared following an established protocol (*55*). Cells were initially fixed with 4% paraformaldehyde in 0.2 M HEPES buffer (1:1 mixture with culture medium) for 5 min at room temperature. The fixative was refreshed twice: 5 min, then 30 min. After washing with 0.1 M HEPES containing 150 mM glycine, cells were permeabilized with 0.001% saponin in 0.1 M HEPES for 5 min. Cells were then incubated with an anti-Flag

Langtaosha (LTS) Preprint doi: https://doi.org/10.65215/LTSpreprints.2026.02.09.000127. This version posted February 9, 2026. The copyright holder for this preprint (which was not certified by peer review) is the author/funder. Creative Commons license: CC Attribution-NonCommercial-NoDerivatives 4.0 https://creativecommons.org/licenses/by-nc-nd/4.0

antibody (Proteintech, 20543-1-AP; 1:100 dilution), followed by five 5-min washes with 0.1 M PBS. Subsequently, cells were incubated overnight at 4 °C with Nanogold goat anti-rabbit IgG (Nanoprobes, 2004; 1:200 dilution). After the washes, samples were post-fixed with 1% glutaraldehyde in 0.2 M HEPES for 30 min and subjected to gold enhancement using GoldEnhance EM Plus (Nanoprobes, 2114) for 2 min. After washing with 1% sodium thiosulfate and distilled water, secondary post-fixation was performed with 1% osmium tetroxide on ice for 1 h, followed by staining with 2% uranyl acetate for 30 min. Dehydration was performed through a graded ethanol series (30%, 50%, 70%, 85%, 95%, and 100%). Infiltration was performed using resin:ethanol mixtures (1:1 for 2 h; 3:1 for 4 h), followed by pure resin under vacuum for 8 h. Polymerization was conducted at 65 °C for 24 h. Ultrathin sections were prepared using an ultramicrotome (Leica, EM UC7) and examined with a transmission electron microscope (FEI, Tecnai G2 Spirit).

Recombinant protein production and pull-down assay

Recombinant proteins were expressed in *Escherichia coli* BL21 cells. Expression was induced with 1 mM isopropyl β-D-1-thiogalactopyranoside, and cultures were incubated at 16 °C or 24 °C for 16–18 h. Cells were harvested by centrifugation and resuspended in either MBP/GST lysis buffer (20 mM Tris-HCl, pH 7.5, 200 mM NaCl, 1 mM EDTA, and 1 mM DTT) or His lysis buffer (50 mM Tris-HCl, pH 8.0, 300 mM NaCl, 4 mM imidazole, and 2 mM β-mercaptoethanol), supplemented with protease inhibitors. Lysates were sonicated on ice, clarified by centrifugation, and incubated with appropriate affinity resins for 3 h at 4 °C. After extensive washing with lysis buffer, bound proteins were eluted using 10 mM maltose (for MBP-tagged proteins) or 240 mM imidazole (for His-tagged proteins).

For pull-down assays, eluted proteins were incubated with GST-tagged fusion proteins immobilized on Glutathione Sepharose 4B beads (GE Healthcare, 17075601) for 2 h at 4 °C. Beads were washed thoroughly and boiled at 100 °C for 8 min. Eluates were separated by SDS-PAGE and analyzed by Coomassie brilliant blue staining and immunoblotting.

Mass spectrometry sample preparation

To identify ATL2 ubiquitination sites under hypoxic conditions, HeLa cells stably expressing 3×Flag-ATL2 in an ATL2 knockout background were cultured under normoxic or hypoxic conditions. Cells were trypsinized, lysed, and centrifuged to obtain clarified supernatants. These lysates were incubated with anti-Flag M2 affinity gel (Millipore, A2220) for 3 h at 4 °C. After thorough washing, bound proteins were eluted by boiling at 100 °C. Immunoprecipitated proteins were separated by SDS–PAGE and visualized with Gel Protein Staining Solution (Meilunbio, MA0399). Gel lanes were excised into slices and subjected to in-gel tryptic digestion. Digested peptides were analyzed using an Orbitrap Fusion Lumos mass spectrometer (Thermo Fisher Scientific) to map post-translational modification sites.

Proximity ligation assay

For proximity ligation assays (PLA), sample preparation, including primary antibodies incubation, followed the immunofluorescence protocol described above, including fixation, permeabilization, and blocking steps. Subsequent procedures were performed using the Duolink In Situ PLA kit (Sigma-Aldrich) according to the manufacturer's instructions. Following two PBS washes, PLA probes were applied to samples for 60 min at 37 °C. Ligation and amplification reactions were carried out for 30 min and 100 min, respectively. Images were acquired using either a Leica TCS SP8 or a ZEISS LSM 980 confocal microscope equipped with a 63×/1.4 NA oil-immersion objective. PLA puncta were manually counted using ImageJ.

Langtaosha (LTS) Preprint doi: https://doi.org/10.65215/LTSpreprints.2026.02.09.000127. This version posted February 9, 2026. The copyright holder for this preprint (which was not certified by peer review) is the author/funder. Creative Commons license: CC Attribution-NonCommercial-NoDerivatives 4.0 https://creativecommons.org/licenses/by-nc-nd/4.0

Statistical analysis

Statistical analyses were performed using GraphPad Prism 8. Data are presented as means, with error bars representing the indicated measures of variation. Sample sizes (n) and specific statistical tests are provided in the figure legends, while P-values are shown directly on the figures. All quantitative experiments were independently repeated at least three times. For multiple-group comparisons, a one-way ANOVA with Tukey's multiple comparisons test was used. For comparisons between two groups, two-tailed Student's t-tests were applied to data that fulfilled assumptions of normality and homogeneity of variance; Welch's t-test was used for data with unequal variances. No statistical method was used to predetermine sample size. In experiments with multiple conditions, cells were randomly assigned to each group.

References

1. D. C. Chan, Mitochondrial dynamics and its involvement in disease. *Annu. Rev. Pathol. Mech. Dis.* **15**, 235–259 (2020).
2. B.-H. Liu, C.-Z. Xu, Y. Liu, Z.-L. Lu, T.-L. Fu, G.-R. Li, Y. Deng, G.-Q. Luo, S. Ding, N. Li, Q. Geng, Mitochondrial quality control in human health and disease. *Mil. Med. Res.* **11**, 32 (2024).
3. W. Chen, H. Zhao, Y. Li, Mitochondrial dynamics in health and disease: mechanisms and potential targets. *Signal Transduct. Target. Ther.* **8**, 333 (2023).
4. A. D. Pilling, D. Horiuchi, C. M. Lively, W. M. Saxton, Kinesin-1 and Dynein are the primary motors for fast transport of mitochondria in Drosophila motor axons. *Mol. Biol. Cell* **17**, 2057–2068 (2006).
5. M. van Spronsen, M. Mikhaylova, J. Lipka, M. A. Schlager, D. J. van den Heuvel, M. Kuijpers, P. S. Wulf, N. Keijzer, J. Demmers, L. C. Kapitein, D. Jaarsma, H. C. Gerritsen, A. Akhmanova, C. C. Hoogenraad, TRAK/Milton motor-adaptor proteins steer mitochondrial trafficking to axons and dendrites. *Neuron* **77**, 485–502 (2013).
6. R. D. Vale, T. S. Reese, M. P. Sheetz, Identification of a novel force-generating protein, kinesin, involved in microtubule-based motility. *Cell* **42**, 39–50 (1985).
7. N. Hirokawa, Y. Noda, Y. Tanaka, S. Niwa, Kinesin superfamily motor proteins and intracellular transport. *Nat. Rev. Mol. Cell Biol.* **10**, 682–696 (2009).
8. Y. Kanai, Y. Okada, Y. Tanaka, A. Harada, S. Terada, N. Hirokawa, KIF5C, a novel neuronal kinesin enriched in motor neurons. *J. Neurosci.* **20**, 6374–6384 (2000).
9. K. Brickley, F. A. Stephenson, Trafficking kinesin protein (TRAK)-mediated transport of mitochondria in axons of hippocampal neurons*. *J. Biol. Chem.* **286**, 18079–18092 (2011).
10. E. E. Glater, L. J. Megeath, R. S. Stowers, T. L. Schwarz, Axonal transport of mitochondria requires milton to recruit kinesin heavy chain and is light chain independent. *J. Cell Biol.* **173**, 545–557 (2006).
11. A. F. MacAskill, K. Brickley, F. A. Stephenson, J. T. Kittler, GTPase dependent recruitment of Grif-1 by Miro1 regulates mitochondrial trafficking in hippocampal neurons. *Mol. Cell. Neurosci.* **40**, 301–312 (2009).
12. X. Guo, G. T. Macleod, A. Wellington, F. Hu, S. Panchumarthi, M. Schoenfield, L. Marin, M. P. Charlton, H. L. Atwood, K. E. Zinsmaier, The GTPase dMiro is required for axonal transport of mitochondria to Drosophila synapses. *Neuron* **47**, 379–393 (2005).
13. A. F. MacAskill, J. T. Kittler, Control of mitochondrial transport and localization in neurons. *Trends Cell Biol.* **20**, 102–112 (2010).
14. Å. Fransson, A. Ruusala, P. Aspenström, The atypical Rho GTPases Miro-1 and Miro-2 have essential roles in mitochondrial trafficking. *Biochem. Biophys. Res. Commun.* **344**, 500–510 (2006).

Langtaosha (LTS) Preprint doi: https://doi.org/10.65215/LTSpreprints.2026.02.09.000127. This version posted February 9, 2026. The copyright holder for this preprint (which was not certified by peer review) is the author/funder. Creative Commons license: CC Attribution-NonCommercial-NoDerivatives 4.0 https://creativecommons.org/licenses/by-nc-nd/4.0

15. D. Lu, Y. Feng, G. Liu, Y. Yang, Y. Ren, Z. Chen, X. Sun, Y. Guan, Z. Wang, Mitochondrial transport in neurons and evidence for its involvement in acute neurological disorders. *Front. Neurosci.* **17**, 1268883 (2023).
16. T. L. Schwarz, Mitochondrial trafficking in neurons. *Cold Spring Harb. Perspect. Biol.* **5**, a011304 (2013).
17. M. Y. Lin, Z. H. Sheng, Regulation of mitochondrial transport in neurons. *Exp. Cell Res.* **334**, 35–44 (2015).
18. A. A. Rowland, G. K. Voeltz, Endoplasmic reticulum–mitochondria contacts: function of the junction. *Nat. Rev. Mol. Cell Biol.* **13**, 607–615 (2012).
19. H. Wu, P. Carvalho, G. K. Voeltz, Here, there, and everywhere: The importance of ER membrane contact sites. *Science* **361**, eaan5835 (2018).
20. A. Larrañaga-SanMiguel, N. Bengoa-Vergniory, H. Flores-Romero, Crosstalk between mitochondria-ER contact sites and the apoptotic machinery as a novel health meter. *Trends Cell Biol.* **35**, 33–45 (2025).
21. O. M. de Brito, L. Scorrano, Mitofusin 2 tethers endoplasmic reticulum to mitochondria. *Nature* **456**, 605–610 (2008).
22. S. Casellas-Díaz, R. Larramona-Arcas, G. Riqué-Pujol, P. Tena-Morraja, C. Müller-Sánchez, M. Segarra-Mondejar, A. Gavaldà-Navarro, F. Villarroya, M. Reina, O. M. Martínez-Estrada, F. X. Soriano, Mfn2 localization in the ER is necessary for its bioenergetic function and neuritic development. *EMBO rep.* **22**, e51954 (2021).
23. V. H. Sathyamurthy, Y. Nagarajan, V. D. Parvathi, Mitochondria-endoplasmic reticulum contact sites (MERCS): A new axis in neuronal degeneration and regeneration. *Mol. Neurobiol.* **61**, 6528–6538 (2024).
24. J. Hu, Y. Shibata, P. P. Zhu, C. Voss, N. Rismanchi, W. A. Prinz, T. A. Rapoport, C. Blackstone, A class of dynamin-like GTPases involved in the generation of the tubular ER network. *Cell* **138**, 549–561 (2009).
25. G. Orso, D. Pendin, S. Liu, J. Tosetto, T. J. Moss, J. E. Faust, M. Micaroni, A. Egorova, A. Martinuzzi, J. A. McNew, A. Daga, Homotypic fusion of ER membranes requires the dynamin-like GTPase atlastin. *Nature* **460**, 978–983 (2009).
26. N. Rismanchi, C. Soderblom, J. Stadler, P. P. Zhu, C. Blackstone, Atlastin GTPases are required for Golgi apparatus and ER morphogenesis. *Hum. Mol. Genet.* **17**, 1591–1604 (2008).
27. J. Hu, T. A. Rapoport, Fusion of the endoplasmic reticulum by membrane-bound GTPases. *Semin. Cell Dev. Biol.* **60**, 105–111 (2016).
28. M. Krols, S. Detry, B. Asselbergh, L. Almeida-Souza, A. Kremer, S. Lippens, R. De Rycke, V. De Winter, F.-J. Müller, I. Kurth, H. T. McMahon, S. N. Savvides, V. Timmerman, S. Janssens, Sensory-neuropathy-causing mutations in ATL3 cause aberrant ER membrane tethering. *Cell Rep.* **23**, 2026–2038 (2018).
29. S. Salinas, C. Proukakis, A. Crosby, T. T. Warner, Hereditary spastic paraplegia: clinical features and pathogenetic mechanisms. *Lancet Neurol.* **7**, 1127–1138 (2008).
30. L. Behrendt, I. Kurth, C. Kaether, A disease causing ATLASTIN 3 mutation affects multiple endoplasmic reticulum-related pathways. *Cell. Mol. Life Sci.* **76**, 1433–1445 (2019).
31. J. Han, H. Park, C. Maharana, A. R. Gwon, J. Park, S. H. Baek, H.-G. Bae, Y. Cho, H. K. Kim, J. H. Sul, J. Lee, E. Kim, J. Kim, Y. Cho, S. Park, L. F. Palomera, T. V. Arumugam, M. P. Mattson, D.-G. Jo, Alzheimer's disease-causing presenilin-1 mutations have deleterious effects on mitochondrial function. *Theranostics* **11**, 8855–8873 (2021).
32. H. Miao, Y. Wang, Y. Huang, H. Zhang, L. Zheng, X. Zhou, X. Wang, Q. Xie, L. Xue, J. Hu, ER fusogens maintain membrane reservoir to ensure brain function. *bioRxiv* 648519 [Preprint] (2025). https://doi.org/10.1101/2025.04.12.648519.

Langtaosha (LTS) Preprint doi: https://doi.org/10.65215/LTSpreprints.2026.02.09.000127. This version posted February 9, 2026. The copyright holder for this preprint (which was not certified by peer review) is the author/funder. Creative Commons license: CC Attribution-NonCommercial-NoDerivatives 4.0 https://creativecommons.org/licenses/by-nc-nd/4.0

33. P. P. Zhu, K. R. Denton, T. M. Pierson, X. J. Li, C. Blackstone, Pharmacologic rescue of axon growth defects in a human iPSC model of hereditary spastic paraplegia SPG3A. *Hum. Mol. Genet.* **23**, 5638–5648 (2014).
34. P. P. Zhu, A. Patterson, B. Lavoie, J. Stadler, M. Shoeb, R. Patel, C. Blackstone, Cellular localization, oligomerization, and membrane association of the hereditary spastic paraplegia 3A (SPG3A) protein atlastin. *J. Biol. Chem.* **278**, 49063–49071 (2003).
35. P. Zheng, C. J. Obara, E. Szczesna, J. Nixon-Abell, K. K. Mahalingan, A. Roll-Mecak, J. Lippincott-Schwartz, C. Blackstone, ER proteins decipher the tubulin code to regulate organelle distribution. *Nature* **601**, 132–138 (2022).
36. S. Bryce, M. Stolzer, D. Crosby, R. Yang, D. Durand, T. H. Lee, Human atlastin-3 is a constitutive ER membrane fusion catalyst. *J. Cell Biol.* **222**, (2023).
37. G. K. Voeltz, W. A. Prinz, Y. Shibata, J. M. Rist, T. A. Rapoport, A class of membrane proteins shaping the tubular endoplasmic reticulum. *Cell* **124**, 573–586 (2006).
38. S. Wang, H. Tukachinsky, F. B. Romano, T. A. Rapoport, Cooperation of the ER-shaping proteins atlastin, lunapark, and reticulons to generate a tubular membrane network. *eLife* **5**, e18605 (2016).
39. Y. Shibata, T. Shemesh, W. A. Prinz, A. F. Palazzo, M. M. Kozlov, T. A. Rapoport, Mechanisms determining the morphology of the peripheral ER. *Cell* **143**, 774–788 (2010).
40. Y. Tanaka, Y. Kanai, Y. Okada, S. Nonaka, S. Takeda, A. Harada, N. Hirokawa, Targeted disruption of mouse conventional kinesin heavy chain, kif5B, results in abnormal perinuclear clustering of mitochondria. *Cell* **93**, 1147–1158 (1998).
41. T. S. Randall, C. Moores, F. A. Stephenson, Delineation of the TRAK binding regions of the kinesin-1 motor proteins. *FEBS Lett.* **587**, 3763–3769 (2013).
42. E. E. Ravitch, E. E. Baltrusaitis, T. A. Perez, K. R. Barrie, A. R. Fenton, E. L. F. Holzbaur, R. Dominguez, Structural-functional characterization of the MIRO1-TRAK1 complex. *Nat. Commun.* **16**, 6173 (2025).
43. M. R. Wieckowski, C. Giorgi, M. Lebiedzinska, J. Duszynski, P. Pinton, Isolation of mitochondria-associated membranes and mitochondria from animal tissues and cells. *Nat. Protoc.* **4**, 1582–1590 (2009).
44. T. Calì, M. Brini, Quantification of organelle contact sites by split-GFP-based contact site sensors (SPLICS) in living cells. *Nat. Protoc.* **16**, 5287–5308 (2021).
45. A. Misko, S. Jiang, I. Wegorzewska, J. Milbrandt, R. H. Baloh, Mitofusin 2 is necessary for transport of axonal mitochondria and interacts with the Miro/Milton complex. *J. Neurosci.* **30**, 4232–4240 (2010).
46. N. Bernard-Marissal, G. van Hameren, M. Juneja, C. Pellegrino, L. Louhivuori, L. Bartesaghi, C. Rochat, O. El Mansour, J.-J. Médard, M. Croisier, C. Maclachlan, O. Poirot, P. Uhlén, V. Timmerman, N. Tricaud, B. L. Schneider, R. Chrast, Altered interplay between endoplasmic reticulum and mitochondria in Charcot–Marie–Tooth type 2A neuropathy. *Proc. Natl. Acad. Sci. U.S.A.* **116**, 2328–2337 (2019).
47. A.-B. Al-Mehdi, V. M. Pastukh, B. M. Swiger, D. J. Reed, M. R. Patel, G. C. Bardwell, V. V. Pastukh, M. F. Alexeyev, M. N. Gillespie, Perinuclear mitochondrial clustering creates an oxidant-rich nuclear domain required for hypoxia-induced transcription. *Sci. Signal.* **5**, ra47–ra47 (2012).
48. Y. Zhao, Z. Feng, Y. Zou, Y. Liu, The E3 ubiquitin ligase SYVN1 ubiquitinates atlastins to remodel the endoplasmic reticulum network. *iScience* **23**, 101494 (2020).
49. N. Yagishita, S. Aratani, C. Leach, T. Amano, Y. Yamano, K. Nakatani, K. Nishioka, T. Nakajima, RING-finger type E3 ubiquitin ligase inhibitors as novel candidates for the treatment of rheumatoid arthritis. *Int. J. Mol. Med.* **30**, 1281–1286 (2012).

Langtaosha (LTS) Preprint doi: https://doi.org/10.65215/LTSpreprints.2026.02.09.000127. This version posted February 9, 2026. The copyright holder for this preprint (which was not certified by peer review) is the author/funder. Creative Commons license: CC Attribution-NonCommercial-NoDerivatives 4.0 https://creativecommons.org/licenses/by-nc-nd/4.0

50. J. R. Friedman, B. M. Webster, D. N. Mastronarde, K. J. Verhey, G. K. Voeltz, ER sliding dynamics and ER–mitochondrial contacts occur on acetylated microtubules. *J. Cell Biol.* **190**, 363–375 (2010).
51. B. Kornmann, C. Osman, P. Walter, The conserved GTPase Gem1 regulates endoplasmic reticulum–mitochondria connections. *Proc. Natl. Acad. Sci. U.S.A.* **108**, 14151–14156 (2011).
52. S. Chen, Y. Sun, Y. Qin, L. Yang, Z. Hao, Z. Xu, M. Björklund, W. Liu, Z. Hong, Dynamic interaction of REEP5–MFN1/2 enables mitochondrial hitchhiking on tubular ER. *J. Cell Biol.* **223**, e202304031 (2024).
53. C. J. Neufeldt, M. Cortese, P. Scaturro, B. Cerikan, J. G. Wideman, K. Tabata, T. Moraes, O. Oleksiuk, A. Pichlmair, R. Bartenschlager, ER-shaping atlastin proteins act as central hubs to promote flavivirus replication and virion assembly. *Nat. Microbiol.* **4**, 2416–2429 (2019).
54. D. Naón, M. I. Hernández-Alvarez, S. Shinjo, M. Wieczor, S. Ivanova, O. Martins de Brito, A. Quintana, J. Hidalgo, M. Palacín, P. Aparicio, J. Castellanos, L. Lores, D. Sebastián, S. Fernández-Veledo, J. Vendrell, J. Joven, M. Orozco, A. Zorzano, L. Scorrano, Splice variants of mitofusin 2 shape the endoplasmic reticulum and tether it to mitochondria. *Science* **380**, eadh9351 (2023).
55. R. S. Polishchuk, A. A. Mironov, Correlative video light/electron microscopy. *Curr. Protoc. Cell Biol.* **11**, 4.8.1–4.8.9 (2001).

Acknowledgments

We are grateful to Dr. Junjie Hu at the National Laboratory of Biomacromolecules, Institute of Biophysics, Chinese Academy of Sciences, for kindly providing the RTN4 KO COS-7 cell line. We extend our thanks to the National Center for Protein Sciences at Peking University in Beijing, China, for assistance. In particular, we thank Liqin Fu, Siying Qin, and Chunyan Shan for confocal microscopy imaging; Jia Luo, Liying Du, and Hongxia Lv for flow cytometry; Dong Liu and Qi Zhang for mass spectrometry; Yingchun Hu and Pengyuan Dong for Immunoelectron microscopy sample preparation and image analysis; and Wei Pan for ultracentrifugation.

Funding: This work was supported by the National Natural Science Foundation of China (32270740, 32130024, 32470735, and 92354306).

Author contributions: Y.C. designed and performed the majority of experiments and drafted the manuscript. P.C. contributed to experimental design and conducted the subcellular fractionation assay. X.P. and Y.C. assisted with molecular biology experiments. P.Z., J.T., and J.C. supervised the project, conceived the study, and provided critical guidance. All authors reviewed, edited, and approved the final version of the manuscript.

Competing interests: The authors declare that they have no competing interests.

Data and materials availability: All data generated in this study are available from the corresponding author upon reasonable request. Biological materials, including plasmids, cell lines, and antibodies, will be available on request. All data needed to evaluate the conclusions in the paper are present in the paper and/or the Supplementary Materials.

Langtaosha (LTS) Preprint doi: https://doi.org/10.65215/LTSpreprints.2026.02.09.000127. This version posted February 9, 2026. The copyright holder for this preprint (which was not certified by peer review) is the author/funder. Creative Commons license: CC Attribution-NonCommercial-NoDerivatives 4.0 https://creativecommons.org/licenses/by-nc-nd/4.0

Figures

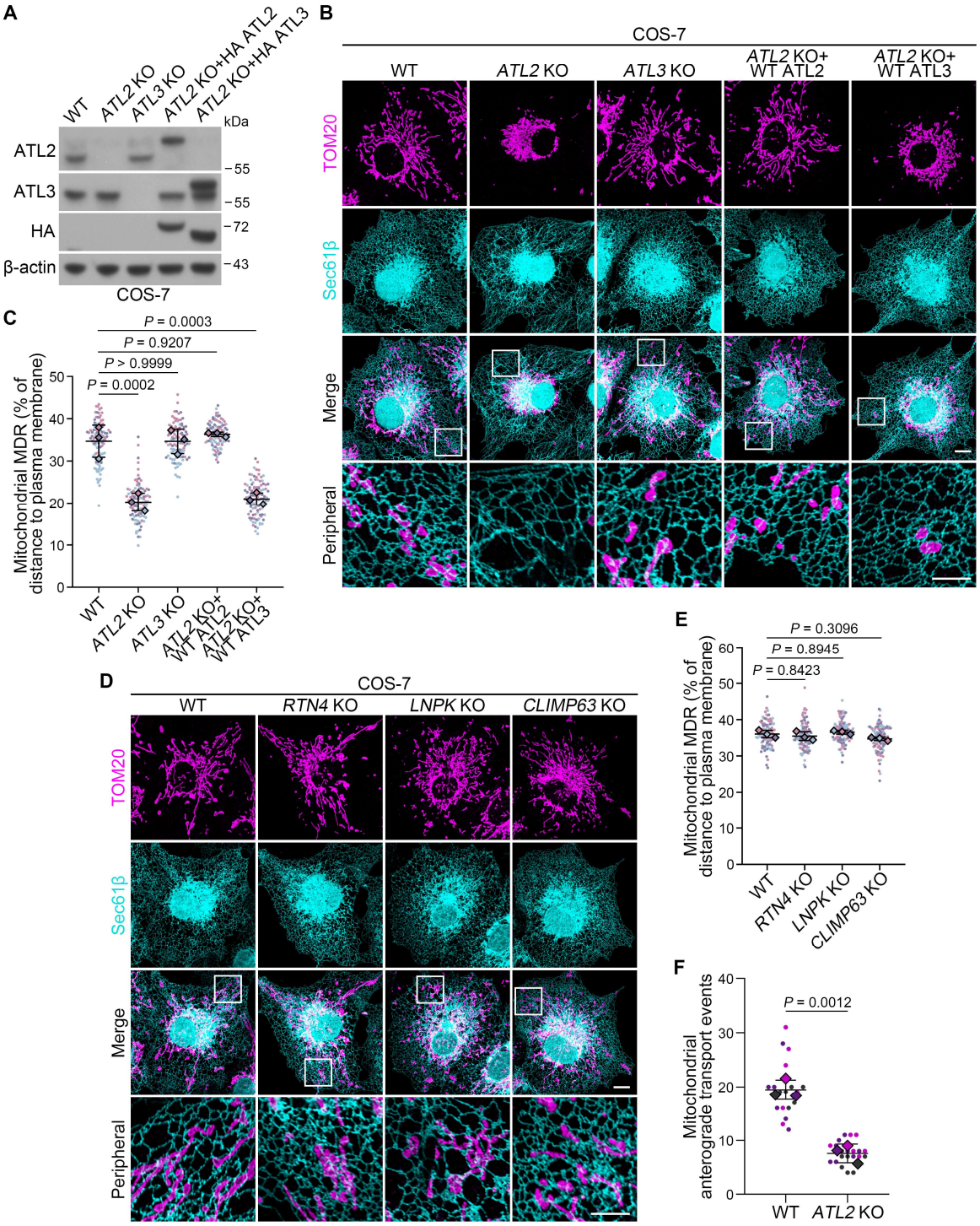

Fig. 1. ATL2 promotes mitochondrial anterograde transport and appropriate distribution.
(**A**) Immunoblot analysis of ATL2 and ATL3 in wild-type (WT), *ATL2* knockout (KO), *ATL3* KO, and *ATL2* KO COS-7 cells stably reconstituted with ATL2 or ATL3.
(**B**) Representative images of cells, genotypes as shown in (A), stably expressing 3×mEmerald-Sec61β (cyan, ER marker) and labelled with TOM20 (magenta, mitochondrial marker). Peripheral regions are enlarged at the bottom. Scale bars, 10 μm; 5 μm (inset).
(**C**) Mitochondrial mean distribution radius (MDR) in cells as shown in (B). n = 102, 104, 103, 104, and 103 cells from three biological replicates. Biological replicates are denoted by color,

Langtaosha (LTS) Preprint doi: https://doi.org/10.65215/LTSpreprints.2026.02.09.000127. This version posted February 9, 2026. The copyright holder for this preprint (which was not certified by peer review) is the author/funder. Creative Commons license: CC Attribution-NonCommercial-NoDerivatives 4.0 https://creativecommons.org/licenses/by-nc-nd/4.0

with individual MDR depicted as smaller points. Data are presented as mean ± s.d. across biological replicates.
(**D**) Representative images of WT, knockout of *RTN4*, *LNPK*, and *CLIMP63* in COS-7 cells stably expressing 3×mEmerald-Sec61β (cyan) and labelled with TOM20 (magenta). Peripheral regions are enlarged at the bottom. Scale bars, 10 μm; 5 μm (inset).
(**E**) Mitochondrial MDR in cells as in (D). n = 104, 102, 104, and 105 cells from three biological replicates. Biological replicates are denoted by color, with individual MDR values depicted as smaller points. Data are presented as mean ± s.d. across biological replicates.
(**F**) Mitochondrial anterograde transport events over 10 min in cells as shown in **fig. S1I**. n = 19 and 21 cells from three biological replicates. Biological replicates are denoted by color, with individual transport events depicted as smaller points. Data are presented as mean ± s.d. across biological replicates. Statistical analyses were performed using ordinary one-way analysis of variance (ANOVA) followed by Tukey's multiple comparisons test (C and E) and two-tailed unpaired *t*-tests (F).

Langtaosha (LTS) Preprint doi: https://doi.org/10.65215/LTSpreprints.2026.02.09.000127. This version posted February 9, 2026. The copyright holder for this preprint (which was not certified by peer review) is the author/funder. Creative Commons license: CC Attribution-NonCommercial-NoDerivatives 4.0 https://creativecommons.org/licenses/by-nc-nd/4.0

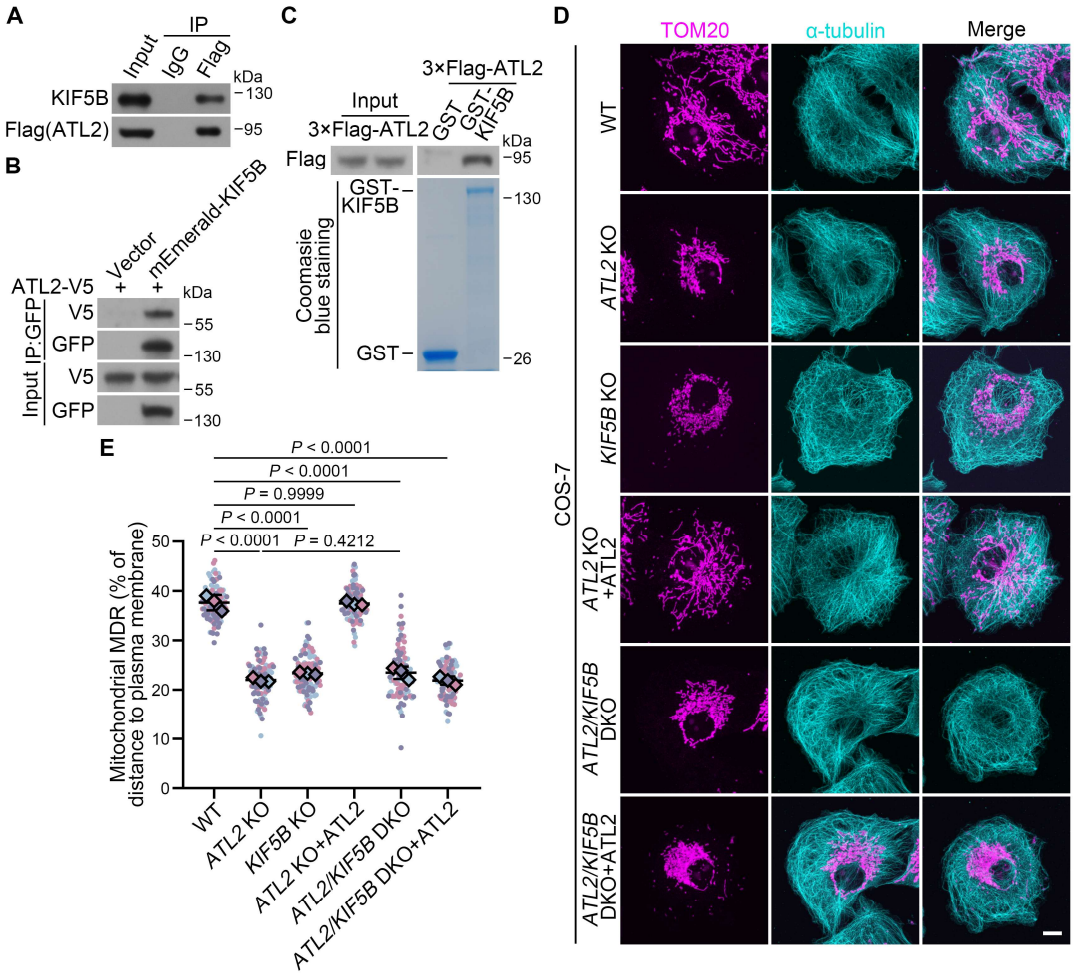

Fig. 2. ATL2 promotes mitochondrial transport and distribution in a KIF5B-dependent manner.

(**A**) Lysates from *ATL2* knockout (KO) HeLa cells stably reconstituted with 3×Flag-ATL2 were subjected to immunoprecipitation (IP) using control IgG or anti-Flag antibody-conjugated beads. Immunoprecipitates were analysed by immunoblotting using antibodies against Flag and KIF5B.

(**B**) HEK293T cells co-transfected with ATL2-V5, and either mEmerald-KIF5B or the mEmerald-C1 vector were subjected to immunoprecipitation using anti-GFP nanobody magarose beads. Immunoprecipitates were analysed by immunoblotting using antibodies against GFP and V5.

(**C**) Lysates from *ATL2* KO HeLa cells expressing 3×Flag-ATL2 were subjected to affinity isolation using immobilized GST or GST-KIF5B. Immunoblots and Coomassie blue-stained gels are shown, probed with antibody against Flag.

(**D**) Representative images of COS-7 cells stained with antibodies against α-tubulin (cyan) and TOM20 (magenta): wild-type (WT), *ATL2* KO, *KIF5B* KO, *ATL2/KIF5B* double knockout (DKO), *ATL2* KO reconstituted with ATL2, and *ATL2/KIF5B* DKO reconstituted with ATL2. Scale bar, 10 μm.

(**E**) Mitochondrial MDR in cells as shown in (D). n = 104, 105, 107, 106, 107, and 105 cells from three biological replicates. Biological replicates are denoted by color, with individual MDR depicted as smaller points. Data are presented as mean ± s.d. across biological replicates. Statistical analyses were performed using ordinary one-way ANOVA followed by Tukey's multiple comparisons test.

Langtaosha (LTS) Preprint doi: https://doi.org/10.65215/LTSpreprints.2026.02.09.000127. This version posted February 9, 2026. The copyright holder for this preprint (which was not certified by peer review) is the author/funder. Creative Commons license: CC Attribution-NonCommercial-NoDerivatives 4.0 https://creativecommons.org/licenses/by-nc-nd/4.0

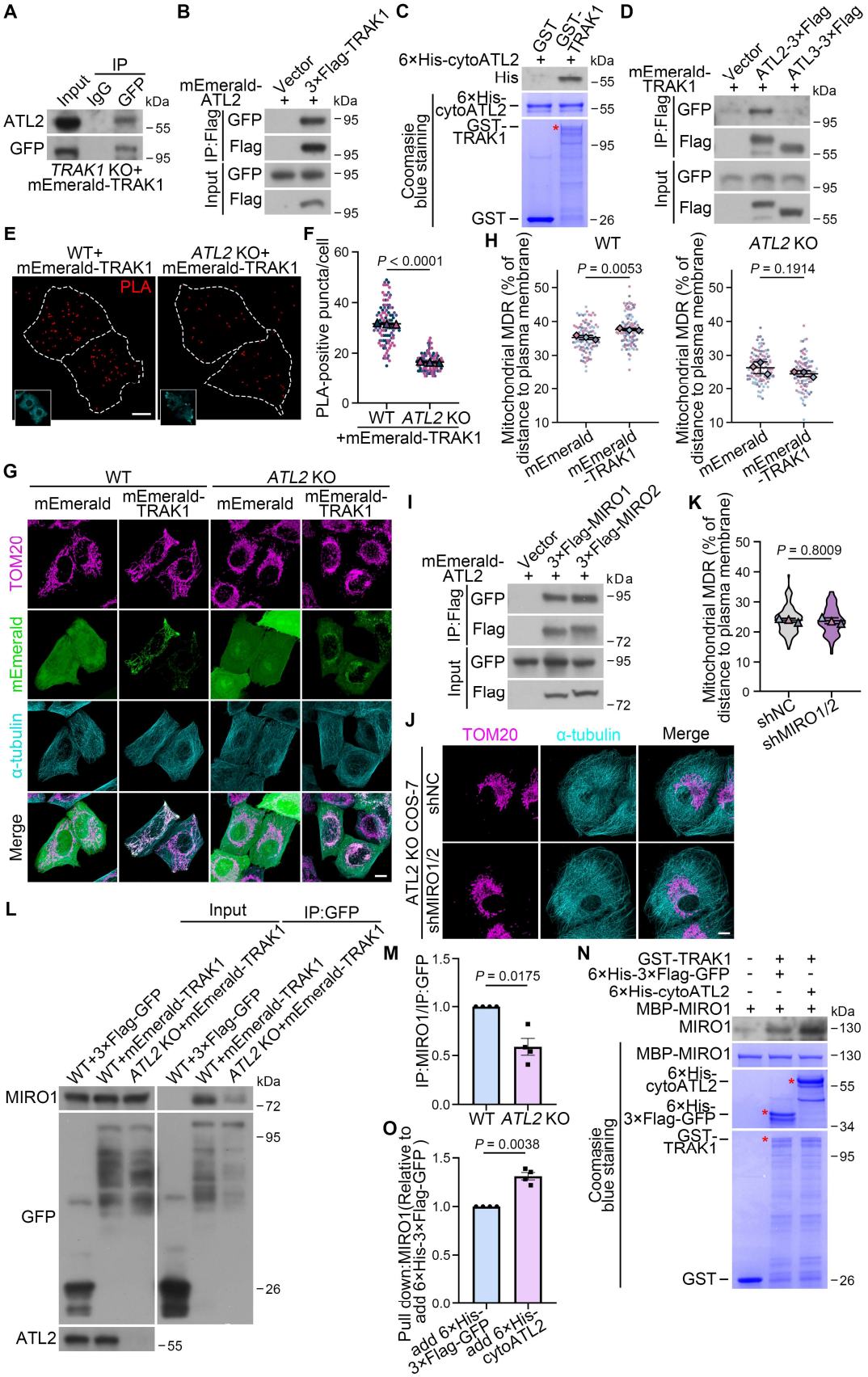

842 **Fig. 3. ATL2 promotes the interaction between TRAK1 and MIRO1.**

843 (**A**) Lysates from *TRAK1* knockout (KO) HeLa cells stably reconstituted with mEmerald-TRAK1

844 were subjected to immunoprecipitation (IP) using control IgG or anti-GFP antibody-conjugated

Langtaosha (LTS) Preprint doi: https://doi.org/10.65215/LTSpreprints.2026.02.09.000127. This version posted February 9, 2026. The copyright holder for this preprint (which was not certified by peer review) is the author/funder. Creative Commons license: CC Attribution-NonCommercial-NoDerivatives 4.0 https://creativecommons.org/licenses/by-nc-nd/4.0

beads. Immunoprecipitates were analysed by immunoblotting using antibodies against GFP and ATL2.
(**B**) HEK293T cells co-transfected with mEmerald-ATL2 and either 3×Flag-TRAK1 or a control vector were subjected to immunoprecipitation using anti-Flag M2 affinity gels. Immunoprecipitates were analysed by immunoblotting using antibodies against Flag and GFP.
(**C**) Purified 6×His-cytoATL2 (residues 1–476) was subjected to affinity isolation using immobilized GST or GST-TRAK1. Immunoblots and Coomassie blue-stained gels are shown, probed with an antibody against His. Asterisk, GST-TRAK1.
(**D**) HEK293T cells co-transfected with mEmerald-TRAK1 and either ATL2-3×Flag or ATL3-3×Flag were subjected to immunoprecipitation using anti-Flag M2 affinity gels. Immunoprecipitates were analysed by immunoblotting using antibodies against Flag and GFP.
(**E**) Proximity ligation assay (PLA) detecting the endogenous interaction between TRAK1 and calnexin in wild-type (WT) and *ATL2* KO HeLa cells reconstituted with mEmerald-TRAK1. Cell outlines (white dotted lines) and mEmerald-TRAK1 (cyan) are indicated. Scale bar, 10 μm.
(**F**) Quantification of PLA puncta per cell as shown in (E). n = 105 and 106 cells from three biological replicates. Biological replicates are denoted by color, with individual PLA puncta depicted as smaller points. Data are presented as mean ± s.d. across biological replicates.
(**G**) WT or *ATL2* KO HeLa cells were transfected with mEmerald-TRAK1 or a control vector and stained with antibodies against α-tubulin (cyan) and TOM20 (magenta). Scale bar, 10 μm.
(**H**) Mitochondrial MDR in cells as shown in (G). n = 106, 106, 107, and 100 cells from three biological replicates. Biological replicates are denoted by color, with individual MDR depicted as smaller points. Data are presented as mean ± s.d. across biological replicates.
(**I**) HEK293T cells co-transfected with mEmerald-ATL2 and either 3×Flag-MIRO1 or 3×Flag-MIRO2 were subjected to immunoprecipitation using anti-Flag M2 affinity gels. Immunoprecipitates were analysed by immunoblotting using antibodies against Flag and GFP.
(**J**) Representative images of *ATL2* KO COS-7 cells with or without additional depletion of MIRO1/2, stained with antibodies against α-tubulin (cyan) and TOM20 (magenta). Scale bar, 10 μm.
(**K**) Mitochondrial MDR in cells as shown in (J). n = 107 and 115 cells from three biological replicates. Biological replicates are denoted by color. Data are presented as mean ± s.d. across biological replicates.
(**L**) Lysates from WT or *ATL2* KO HeLa cells stably expressing mEmerald-TRAK1, or WT cells expressing 3×Flag-GFP, were incubated with anti-GFP nanobody magarose beads. Immunoprecipitates were analysed by immunoblotting ueing antibodies against GFP, MIRO1, and ATL2.
(**M**) Quantification of relative intensity in (L), with data from four biological replicates presented as mean ± s.e.m.
(**N**) *In vitro* pull-down assay with purified proteins. Immobilized GST or GST-TRAK1 was incubated with MBP-MIRO1 and 6×His-cytoATL2 or 6×His-3×Flag-GFP, followed by immunoblotting for MIRO1 and Coomassie staining (asterisks, key protein bands).
(**O**) Quantification of relative MIRO1 intensity as shown in (N), with data from four biological replicates presented as mean ± s.e.m. Statistical analyses were performed using two-tailed unpaired *t*-tests with (M and O) or without (F, H, and K) Welch's correction.

Langtaosha (LTS) Preprint doi: https://doi.org/10.65215/LTSpreprints.2026.02.09.000127. This version posted February 9, 2026. The copyright holder for this preprint (which was not certified by peer review) is the author/funder. Creative Commons license: CC Attribution-NonCommercial-NoDerivatives 4.0 https://creativecommons.org/licenses/by-nc-nd/4.0

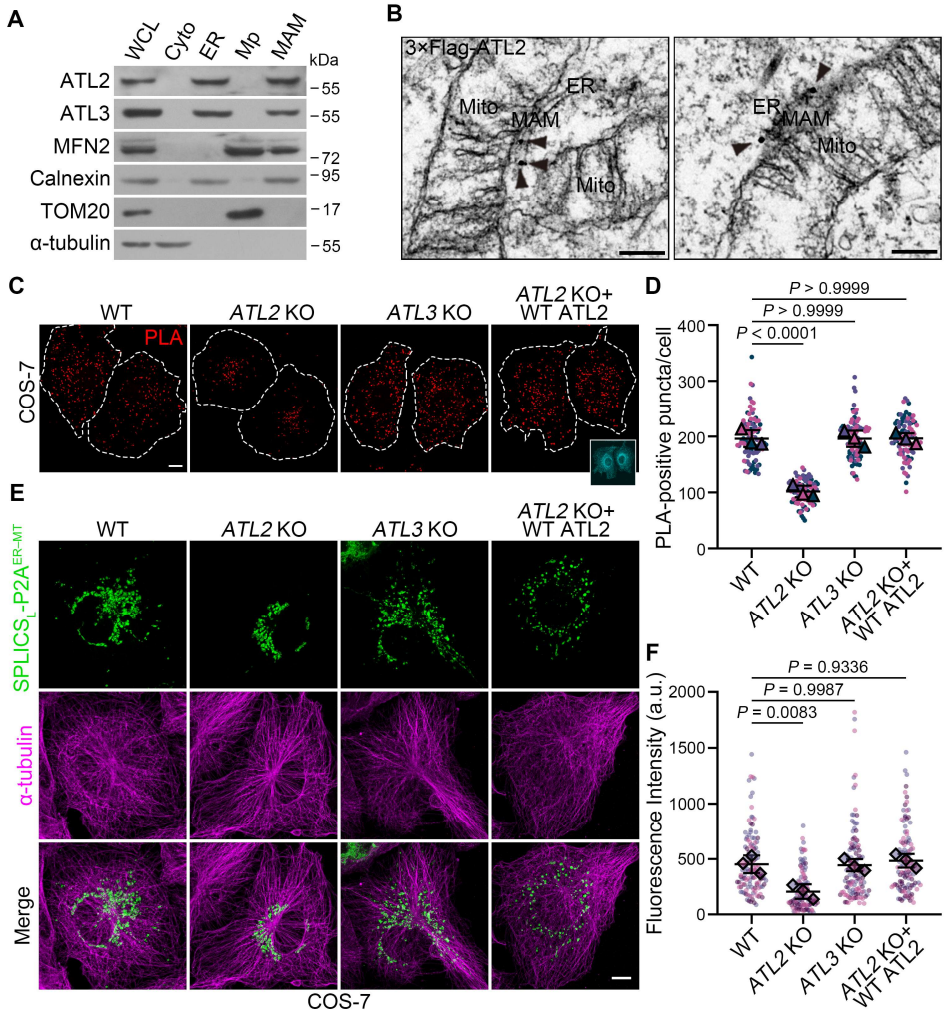

Fig. 4. ATL2 is required for maintaining ER–mitochondria contact sites.
(**A**) Immunoblot analysis of subcellular fractions from mouse liver. WCL, whole-cell lysate; Cyto, cytosol; ER, endoplasmic reticulum; Mp, purified mitochondria; MAM, mitochondria-associated ER membranes.
(**B**) Immunogold electron microscopy of *ATL2* knockout (KO) HeLa cells stably expressing 3×Flag-ATL2. Arrowheads mark gold particles labelling 3×Flag-ATL2 at the MAM. Scale bar, 200 nm.
(**C**) PLA detecting the endogenous interaction between TOM20 and calnexin in wild-type (WT), *ATL2* KO, *ATL3* KO and *ATL2* KO reconstituted with ATL2 COS-7 cells. Cell outlines (white dotted lines) and expressed ATL2 (cyan) are indicated. Scale bar, 10 μm.
(**D**) Quantification of PLA puncta per cell as shown in (C). n = 95, 91, 93, and 91 cells from three biological replicates. Biological replicates are denoted by color, with individual PLA puncta depicted as smaller points. Data are presented as mean ± s.d. across biological replicates.
(**E**) Representative images of WT, *ATL2* KO, *ATL3* KO and *ATL2* KO reconstituted with ATL2 COS-7 cells expressing $SPLICS_L$-$P2A^{ER\text{-}MT}$ (green) and stained with antibodies against α-tubulin (magenta). Scale bar, 10 μm.
(**F**) Quantification of green fluorescence intensity per cell area as shown in (E). n = 120, 112, 120, and 112 cells from three biological replicates. Biological replicates are denoted by color, with individual data points depicted as smaller points. Data are presented as mean ± s.d. across biological replicates. In (D) and (F), statistical analyses were performed using ordinary one-way ANOVA followed by Tukey's multiple comparisons test.

Langtaosha (LTS) Preprint doi: https://doi.org/10.65215/LTSpreprints.2026.02.09.000127. This version posted February 9, 2026. The copyright holder for this preprint (which was not certified by peer review) is the author/funder. Creative Commons license: CC Attribution-NonCommercial-NoDerivatives 4.0 https://creativecommons.org/licenses/by-nc-nd/4.0

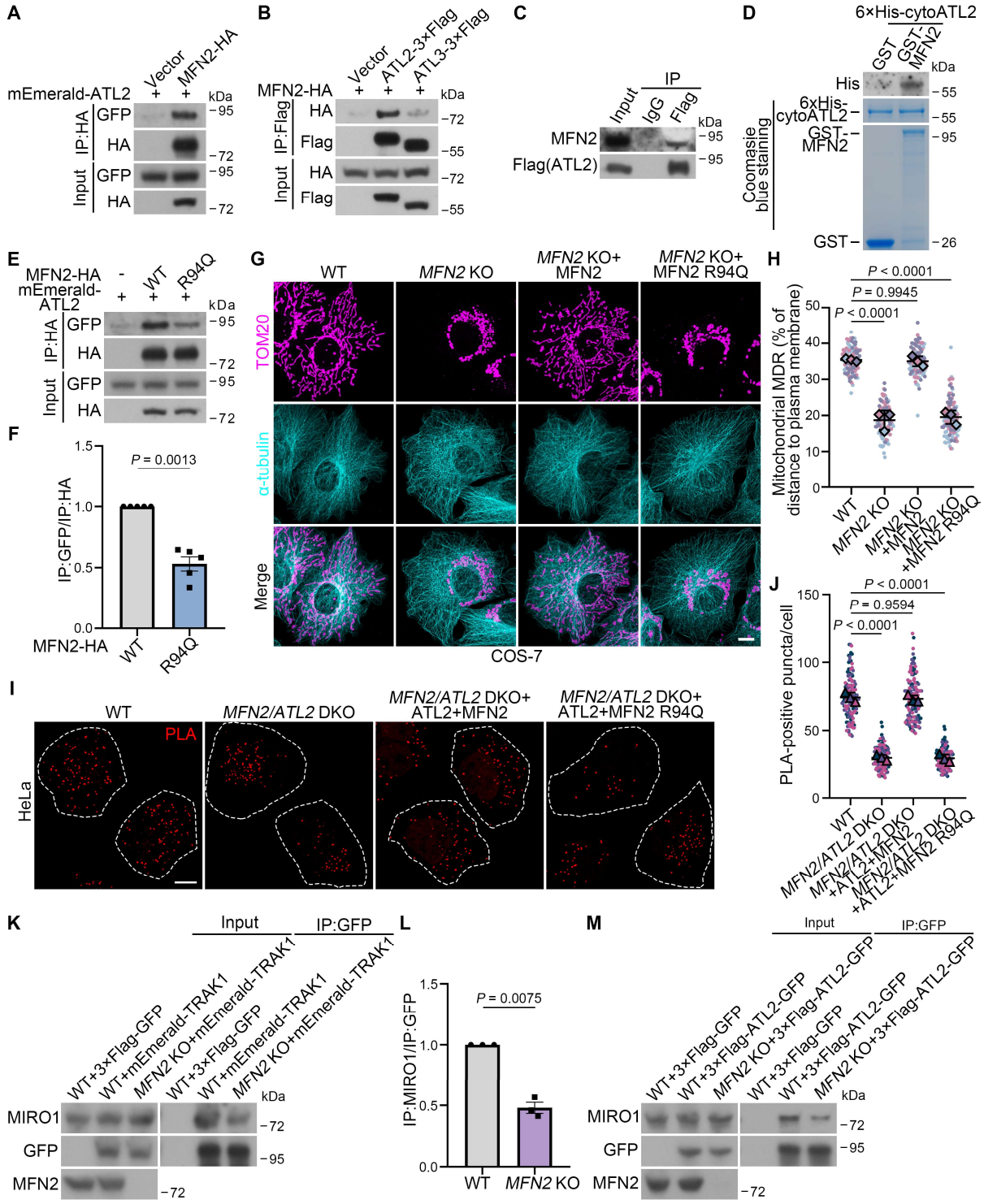

Fig. 5. The ATL2–MFN2 interaction is required for mitochondrial transport.
(**A**) HEK293T cells co-transfected with mEmerald-ATL2 and either MFN2-HA or a control vector, were subjected to immunoprecipitation (IP) using anti-HA nanobody magarose beads. Immunoprecipitates were analysed by immunoblotting using antibodies against HA and GFP. (**B**) HEK293T cells co-transfected with MFN2-HA together with either ATL2-3×Flag or ATL3-3×Flag were subjected to immunoprecipitation using anti-Flag M2 affinity gels. Immunoprecipitates were analysed by immunoblotting using antibodies against Flag and HA.

Langtaosha (LTS) Preprint doi: https://doi.org/10.65215/LTSpreprints.2026.02.09.000127. This version posted February 9, 2026. The copyright holder for this preprint (which was not certified by peer review) is the author/funder. Creative Commons license: CC Attribution-NonCommercial-NoDerivatives 4.0 https://creativecommons.org/licenses/by-nc-nd/4.0

(**C**) Lysates from *ATL2* knockout (KO) HeLa cells stably reconstituted with 3×Flag-ATL2 were subjected to immunoprecipitation using control IgG or anti-Flag antibody-conjugated beads. Immunoprecipitates were analysed by immunoblotting using antibodies against Flag and MFN2.
(**D**) Purified 6×His-cytoATL2 (residues 1–476) was subjected to affinity isolation using immobilized GST or GST-MFN2. Immunoblots and Coomassie blue-stained gels are shown, probed with an antibody against His.
(**E**) HEK293T cells co-transfected with mEmerald-ATL2 together, and either MFN2-HA or MFN2 R94Q-HA were subjected to immunoprecipitation using anti-HA nanobody magarose beads. Immunoprecipitates were analysed by immunoblotting using antibodies against HA and GFP.
(**F**) Quantification of relative intensity as shown in (E), with data from five biological replicates presented as mean ± s.e.m.
(**G**) Representative images of wild-type (WT), *MFN2* KO, and *MFN2* KO COS-7 cells reconstituted with WT MFN2 or MFN2 R94Q stained with antibodies against α-tubulin (cyan) and TOM20 (magenta). Scale bar, 10 μm.
(**H**) Mitochondrial MDR in cells as shown in (G). n = 107, 106, 107, and 107 cells from three biological replicates. Biological replicates are denoted by color, with individual MDR values depicted as smaller points. Data are presented as mean ± s.d. across biological replicates.
(**I**) PLA detecting the endogenous interaction between TOM20 and calnexin in WT, *MFN2* KO, *MFN2/ATL2* double knockout (DKO), and DKO HeLa cells reconstituted with ATL2 together with either WT MFN2 or MFN2 R94Q. Cell outlines (white dotted lines) are indicated. Scale bar, 10 μm.
(**J**) Quantification of PLA puncta per cell as shown in (I). n = 125 cells from three biological replicates. Biological replicates are denoted by color, with individual PLA puncta depicted as smaller points. Data are presented as mean ± s.d. across biological replicates.
(**K**) Lysates from WT or *MFN2* KO HeLa cells stably expressing mEmerald-TRAK1, or WT cells expressing 3×Flag-GFP, were incubated with anti-GFP nanobody magarose beads. Immunoprecipitates were analysed by immunoblotting using antibodies against GFP, MIRO1, and MFN2.
(**L**) Quantification of relative intensity as shown in (K), with data from three biological replicates presented as mean ± s.e.m.
(**M**) Lysates from WT or *MFN2* KO HeLa cells stably expressing 3×Flag-ATL2-GFP, or WT cells expressing 3×Flag-GFP, were incubated with anti-GFP nanobody magarose beads. Immunoprecipitates were analysed by immunoblotting using antibodies against GFP, MIRO1, and MFN2. Statistical analyses were performed using two-tailed unpaired *t*-tests with Welch's correction (F and L) and ordinary one-way ANOVA followed by Tukey's multiple comparisons test (H and J).

Langtaosha (LTS) Preprint doi: https://doi.org/10.65215/LTSpreprints.2026.02.09.000127. This version posted February 9, 2026. The copyright holder for this preprint (which was not certified by peer review) is the author/funder. Creative Commons license: CC Attribution-NonCommercial-NoDerivatives 4.0 https://creativecommons.org/licenses/by-nc-nd/4.0

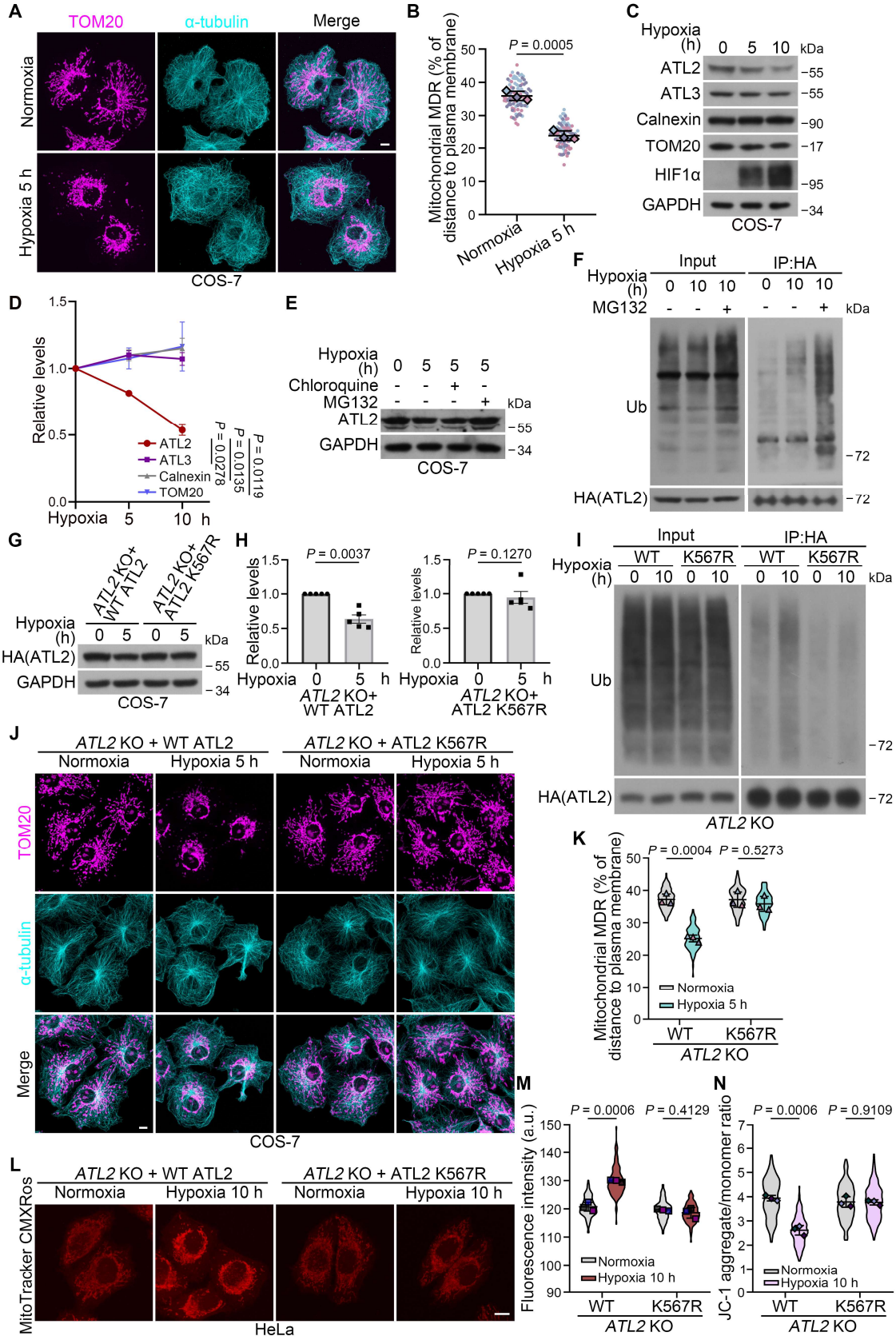

Fig. 6. Hypoxia induces ATL2 degradation, leading to mitochondrial clustering.

(**A**) Representative images of COS-7 cells exposed to 1% O_2 for the indicated times and stained with antibodies against α-tubulin (cyan) and TOM20 (magenta). Scale bar, 10 μm.

Langtaosha (LTS) Preprint doi: https://doi.org/10.65215/LTSpreprints.2026.02.09.000127. This version posted February 9, 2026. The copyright holder for this preprint (which was not certified by peer review) is the author/funder. Creative Commons license: CC Attribution-NonCommercial-NoDerivatives 4.0 https://creativecommons.org/licenses/by-nc-nd/4.0

(**B**) Mitochondrial MDR in cells as shown in (A). *n* = 102 cells from three biological replicates. Biological replicates are denoted by color, with individual MDR values depicted as smaller points. Data are presented as mean ± s.d. across biological replicates.
(**C**) Immunoblot analysis of ATL2, ATL3, calnexin, and TOM20 in COS-7 cells exposed to 1% O_2 for the indicated times.
(**D**) Quantification of relative protein levels following 10 h of hypoxia as shown in (C), with data from three biological replicates presented as mean ± s.e.m.
(**E**) Immunoblot analysis of ATL2 in COS-7 cells exposed to 1% O_2 for the indicated times in the presence of MG132 (10 μM) or chloroquine (10 μM).
(**F**) Lysates from *ATL2* knockout (KO) HeLa cells stably expressing HA-ATL2 exposed to 1% O_2 for the indicated times with or without MG132 (10 μM) were subjected to immunoprecipitation (IP) using anti-HA beads, followed by immunoblotting using antibodies against HA and ubiquitin (Ub).
(**G**) Immunoblot analysis of HA protein levels in *ATL2* KO COS-7 cells stably expressing HA-WT ATL2 or HA-ATL2 K567R, exposed to 1% O_2 for the indicated times.
(**H**) Quantification of relative protein levels as shown in (G), with data from five biological replicates presented as mean ± s.e.m.
(**I**) Lysates from *ATL2* KO HeLa cells stably expressing HA-WT ATL2 or HA-ATL2 K567R, exposed to 1% O_2 for 0 or 10 h, were subjected to immunoprecipitation using anti-HA beads, followed by immunoblotting using antibodies against HA and Ub.
(**J**) Representative images of *ATL2* KO COS-7 cells stably expressing WT ATL2 or the ATL2 K567R mutant, exposed to 1% O_2 for 0 or 5 h, stained with antibodies against α-tubulin (cyan) and TOM20 (magenta). Scale bar, 10 μm.
(**K**) Mitochondrial MDR in cells as shown in (J). *n* = 105, 105, 104, and 105 cells from three biological replicates. Biological replicates are denoted by color. Data are presented as mean ± s.d. across biological replicates.
(**L**) Representative images of *ATL2* KO HeLa cells stably expressing WT ATL2 or the ATL2 K567R mutant, exposed to 1% O_2 for 0 or 10 h, stained with MitoTracker Red CMXRos (100 μM). Scale bar, 10 μm.
(**M**) Quantification of fluorescence intensity per cell area as shown in (L). *n* = 116, 116, 115, and 118 cells from three biological replicates. Biological replicates are denoted by color. Data are presented as mean ± s.d. across biological replicates.
(**N**) Quantification of the JC-1 aggregate/monomer ratio as shown in **fig. S7E**. *n* = 150 cells from three biological replicates. Biological replicates are denoted by color. Data are presented as mean ± s.d. across biological replicates. Statistical analyses were performed using ordinary one-way ANOVA followed by Tukey's multiple comparisons test (D) and two-tailed unpaired *t*-tests with (H) or without (B, K, M, and N) Welch's correction.

Langtaosha (LTS) Preprint doi: https://doi.org/10.65215/LTSpreprints.2026.02.09.000127. This version posted February 9, 2026. The copyright holder for this preprint (which was not certified by peer review) is the author/funder. Creative Commons license: CC Attribution-NonCommercial-NoDerivatives 4.0 https://creativecommons.org/licenses/by-nc-nd/4.0

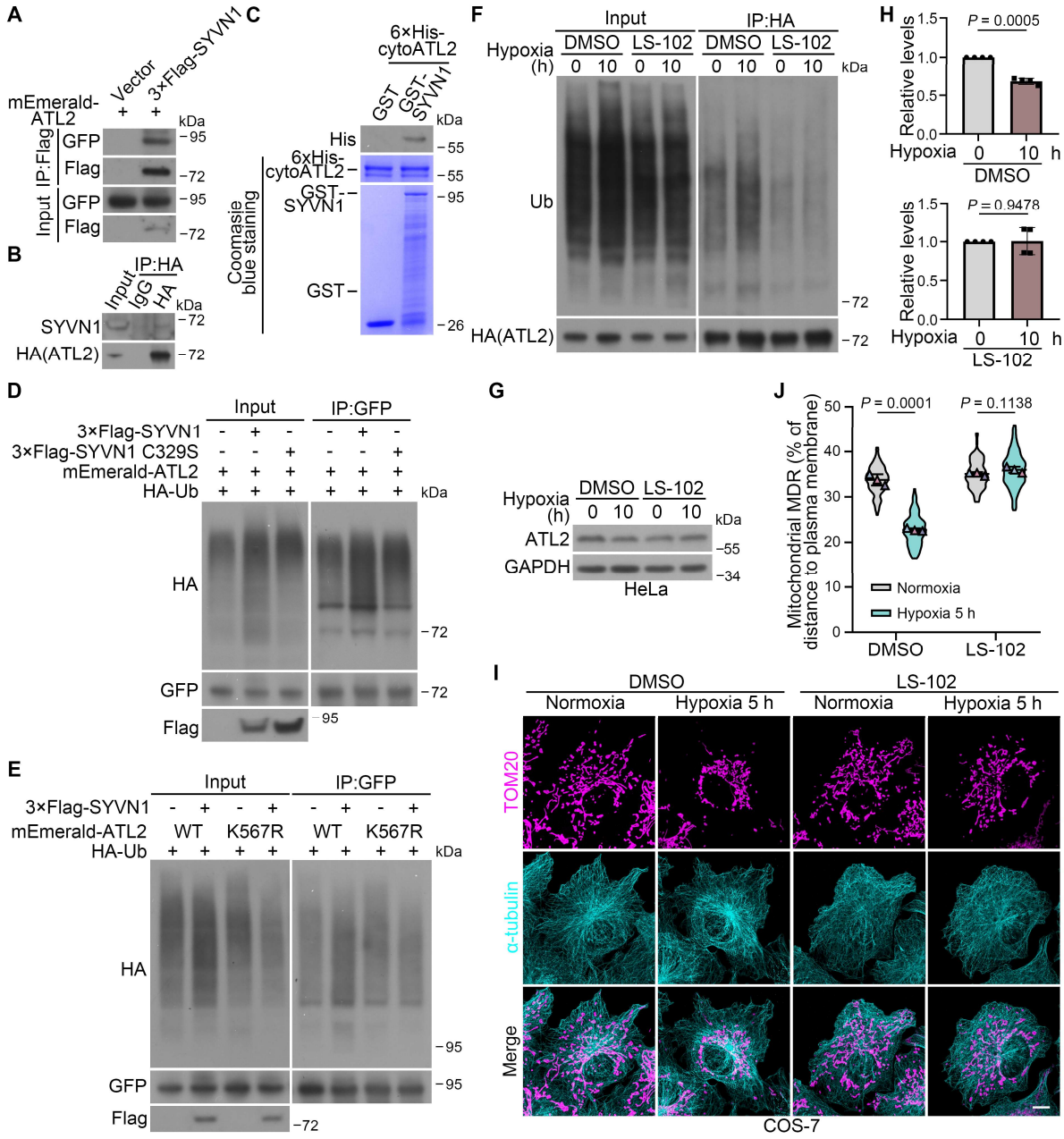

Fig. 7. SYVN1 is responsible for ATL2 ubiquitination under hypoxia.

(**A**) HEK293T cells co-transfected with mEmerald-ATL2 and either 3×Flag-SYVN1 or a control vector were subjected to immunoprecipitation (IP) using anti-Flag M2 affinity gels. Immunoprecipitates were analysed by immunoblotting using antibodies against Flag and GFP.

(**B**) Lysates from *ATL2* knockout (KO) HeLa cells stably reconstituted with HA-ATL2 were subjected to immunoprecipitation using control IgG or anti-HA antibody-conjugated beads. Immunoprecipitates were analysed by immunoblotting using antibodies against HA and SYVN1.

(**C**) Purified 6×His-cytoATL2 (residues 1–476) was subjected to affinity isolation using immobilized GST or GST-SYVN1. Immunoblots and Coomassie blue-stained gels are shown, probe with an antibody against His.

(**D**) HEK293T cells co-transfected with mEmerald-ATL2, HA-Ubiquitin (Ub), together with either 3×Flag-SYVN1 or the 3×Flag-SYVN1 C329S mutant, were subjected to immunoprecipitation using anti-GFP nanobody magarose beads. Immunoprecipitates were analysed by immunoblotting using antibodies against GFP, HA, and Flag.

Langtaosha (LTS) Preprint doi: https://doi.org/10.65215/LTSpreprints.2026.02.09.000127. This version posted February 9, 2026. The copyright holder for this preprint (which was not certified by peer review) is the author/funder. Creative Commons license: CC Attribution-NonCommercial-NoDerivatives 4.0 https://creativecommons.org/licenses/by-nc-nd/4.0

(E) HEK293T cells co-transfected with HA-Ub, mEmerald-ATL2 (WT and K567R), together with either 3×Flag-SYVN1 or a control vector, were subjected to immunoprecipitation using anti-GFP nanobody magarose beads. Immunoprecipitates were analysed by immunoblotting using antibodies against GFP, HA, and Flag.
(**F**) Lysates from *ATL2* KO HeLa cells stably expressing HA-ATL2, exposed to 1% O_2 for the indicated times with or without LS-102 (20 μM), were subjected to immunoprecipitation using anti-HA beads, followed by immunoblotting using antibodies against HA and Ub.
(**G**) Immunoblot analysis of ATL2 protein levels in HeLa cells exposed to 1% O_2 for the indicated times with or without LS-102 (20 μM).
(**H**) Quantification of relative protein levels as shown in (G), with data from four biological replicates presented as mean ± s.e.m.
(**I**) Representative images of COS-7 cells exposed to 1% O_2 for the indicated times with or without LS-102 (20 μM), stained with antibodies against α-tubulin (cyan) and TOM20 (magenta). Scale bar, 10 μm.
(**J**) Mitochondrial MDR in cells as shown in (I). n = 101, 101, 100, and 103 cells from three biological replicates. Biological replicates are denoted by color. Data are presented as mean ± s.d. across biological replicates. Statistical analyses were performed using two-tailed unpaired *t*-tests with (H) or without (J) Welch's correction.

Langtaosha (LTS) Preprint doi: https://doi.org/10.65215/LTSpreprints.2026.02.09.000127. This version posted February 9, 2026. The copyright holder for this preprint (which was not certified by peer review) is the author/funder. Creative Commons license: CC Attribution-NonCommercial-NoDerivatives 4.0 https://creativecommons.org/licenses/by-nc-nd/4.0

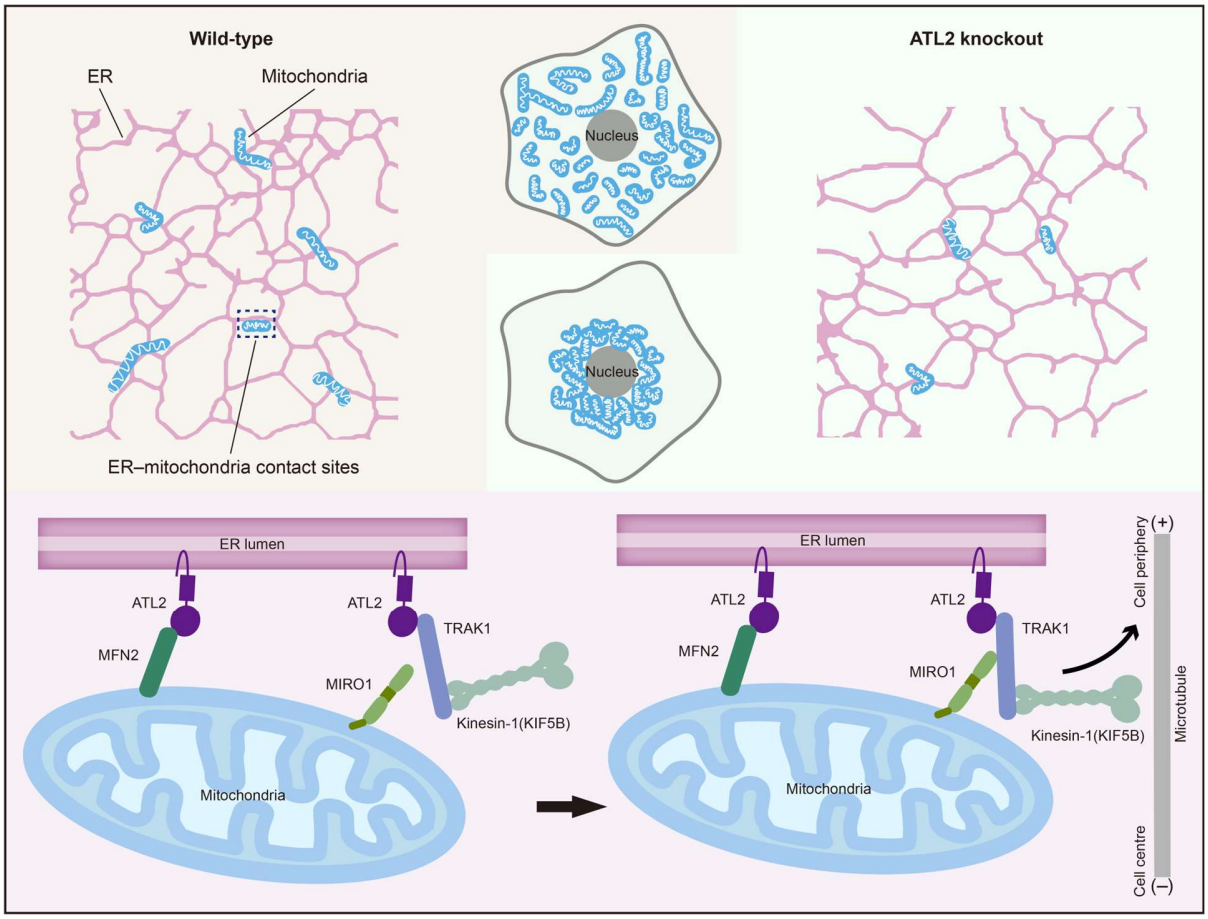

Fig. 8. ER–mitochondria contacts orchestrate mitochondrial transport via ATL2. The ER protein ATL2 promotes the TRAK1–MIRO1 interaction by recruiting TRAK1 to the ER and by interacting with mitochondrial MFN2 at contact sites. This facilitates assembly of the transport adaptor complex, which in turn recruits the motor protein KIF5B to drive anterograde mitochondrial transport.